remote sensing

MDPI

Review

Multi-Mission GNSS Radio Occultation at NOAA/STAR: A Review of Commercial Data Quality, Weather and Climate Applications, and an Outlook on Future Priorities

Shu-peng Ho [1,*], William Miller [2], Xi Shao [2], Jun Zhou [3], Xinjia Zhou [3], Guojun Gu [2], Yong Chen [1], Xin Jing [2] and Tung-Chang Liu [2]

[1] NOAA National Environmental Satellite, Data, and Information Service, Center for Satellite Applications and Research, College Park, MD 20740, USA; yong.chen@noaa.gov
[2] Cooperative Institute for Satellite Earth System Studies (CISESS), Earth System Science Interdisciplinary Center, University of Maryland, College Park, MD 20740, USA; william.miller@noaa.gov (W.M.); xi.shao@noaa.gov (X.S.); ggu@umd.edu (G.G.); xin.jing@noaa.gov (X.J.); tcliu@umd.edu (T.-C.L.)
[3] Entarian LLC, Greenbelt, MD 20770, USA; jun.zhou@noaa.gov (J.Z.); xinjia.zhou@noaa.gov (X.Z.)
* Correspondence: shu-peng.ho@noaa.gov; Tel.: +1-301-683-3596

Highlights

What are the main findings?

- Cross-mission performance is best evaluated along a conditional pathway from orbit and viewing geometry through antenna gain and received signal, SNR and tracking, penetration and phase quality, retrieval bias and uncertainty, and application-specific value; mean SNR alone is not a sufficient measure of mission quality.
- Commercial Spire and PlanetiQ observations are broadly compatible with COSMIC-2 and NOAA partners' missions in the neutral atmosphere, while their additional profiles improve sampling and provide incremental value for numerical weather prediction.

What are the implications of the main findings?

- Mission evaluation should trace each link in this pathway while distinguishing signal quality, retrieval quality and uncertainty, quality-controlled usable yield, sampling complementarity, and application-specific impact.
- The principal outlook priorities are uncertainty-aware quality control, improved lower-tropospheric retrievals, common multi-mission reprocessing, stability assessment, and observing-system designs that balance measurement quality with coverage.

Abstract

Global Navigation Satellite System (GNSS) radio occultation (RO) has evolved into a heterogeneous multi-mission observing system that combines national, international partner, and commercial constellations. This review and outlook synthesize NOAA/STAR assessments of GNSS RO commercial data, including Spire and PlanetiQ, and compare their quality with those of national missions, COSMIC-2, MetOp, and other missions. We emphasize the results in the neutral atmosphere. To examine heterogeneous multiple RO missions, we organized the comparisons along a pathway from (i) orbit and viewing geometry through antenna gain and received signal, (ii) examining their signal-to-noise ratio (SNR) and penetration, (iii) quantifying the phase quality, retrieval bias and uncertainty, (iv) demonstrating their impacts on numerical weather prediction (NWP),

Academic Editors: Carmine Serio

Received: 1 September 2026
Revised: 28 October 2026
Accepted: 2 November 2026
Published: 6 November 2026

Copyright: © 2026 by the authors. Licensee MDPI, Basel, Switzerland. This article is an open access article distributed under the terms and conditions of the Creative Commons Attribution (CC BY) license.

and climate and environmental applications. The reviewed comparisons show that higher SNR generally improves tracking and lower-tropospheric penetration but does not by itself remove biases and uncertainty arising from water-vapor irregularity, multipath, super-refraction, departures from spherical symmetry, or processing choices. Spire and PlanetiQ retrievals are broadly compatible with COSMIC-2 and international missions in the principal atmospheric layers, and their additional profiles improve spatiotemporal sampling and provide incremental value for global and tropical-cyclone prediction. For long-term environmental records, however, operational usefulness is not sufficient: common processing, inter-mission stability assessment, sampling correction, and mission-specific uncertainty characterization are required. Multi-mission RO observations support upper-troposphere and lower-stratosphere temperature records, tropospheric water-vapor variability and trend analyses, and planetary-boundary-layer height estimates when these conditions are met. The synthesis yields an application-conditioned evaluation framework that separates signal quality, retrieval quality, usable observation yield, sampling complementarity, and downstream impact. The principal outlook priorities are uncertainty-aware quality control and error specification, improved treatment of super-refraction and lower-tropospheric retrievals, sustained multi-mission reprocessing and intercomparison, and observing-system design that balances measurement quality with coverage.

Keywords: GNSS radio occultation; COSMIC-2; commercial radio occultation; multi-mission consistency; signal-to-noise ratio; numerical weather prediction; climate monitoring; planetary boundary layer; observation uncertainty; outlook

1. Introduction

Global Navigation Satellite System (GNSS) radio occultation (RO) has entered a heterogeneous multi-mission era. Between 2016 and August 2026, at least eight RO missions or mission series were launched: COSMIC-2, Spire, PlanetiQ, GeoOptics, Sentinel-6, YunYao, Fengyun-3, and Tianmu. As of August 2026, approximately 100 GNSS RO sensors were operating in orbit and tracking signals from GPS, GLONASS, Galileo, BeiDou, QZSS, NavIC/IRNSS, and GPS III. These all-weather observations support atmospheric science, numerical weather prediction (NWP), extreme-weather detection, environmental monitoring, and space-weather studies [1–5].

NOAA has included GNSS RO among its key observables since 2006 [6–8]. Since then, NCEP has assimilated data from partner missions, including MetOp-A/-B/-C, KOMPSAT-5, PAZ, TerraSAR-X, and the Taiwan-U.S. FORMOSAT-3/Constellation Observing System for Meteorology, Ionosphere, and Climate mission (COSMIC-1, see Figure 1). COSMIC-2 is the follow-on mission to COSMIC-1 [7,9]. In 2019, NCEP began assimilating approximately 5000 COSMIC-2 RO profiles into its global NWP system.

To incorporate additional GNSS RO observations into the NCEP NWP system, NOAA began planning commercial RO procurement in 2016. In addition to national or international partner missions such as COSMIC-2 and the MetOp series, commercial RO observations are provided by CubeSat constellations (e.g., Spire) and SmallSat constellations (e.g., PlanetiQ). From 2016 to 2019, NOAA conducted two pilot studies under the Commercial Weather Data Program (CWDP), acquiring RO data from GeoOptics and Spire Global. Based on these studies, NOAA initiated the Radio Occultation Data Buy (RODB) delivery orders. As of August 2026, NOAA purchases up to 10,000 RO profiles per day—7000 from PlanetiQ and 3000 from Spire—under RODB-2 (Table 1 and Figure 1). Table 1 summarizes the commercial RO data examined during the

pilot studies and RODB delivery periods. NOAA began purchasing PlanetiQ RO data under RODB-1 and continued these purchases under RODB-2.

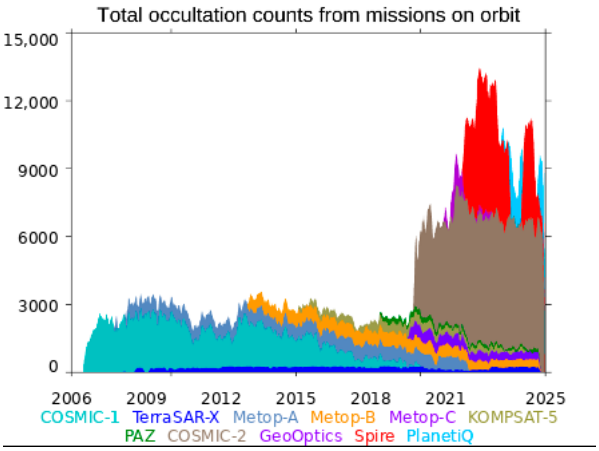


Figure 1. Total occultation counts from in-orbit missions used by NCEP since 2006.

Table 1. Timeline of NOAA commercial RO data-purchase periods.

Program/Delivery Order (DO)	Period	Major Vendors
CWDP Round 1/2	2016–2019	GeoOptics and Spire Global
RODB-1 (DO-1 to DO-4)	2020–2022	GeoOptics, Spire Global, and PlanetiQ
RODB-2 (DO-5)	2023–2028	Spire Global and PlanetiQ

However, commercial and nationally funded missions differ in orbital and viewing geometry, which may affect the antenna gain pattern and lead to differences in measurement uncertainty (i.e., signal-to-noise ratio (SNR)) and, in turn, retrieval uncertainty. These differences have raised concerns within the RO community about whether commercial-mission data quality differs from that of nationally funded missions and whether these differences present additional challenges for using GNSS RO data in NWP and atmospheric applications. The primary questions are:

(1) What evaluation pathway can we use to examine current heterogeneous multi-RO missions, from viewing geometry and signal sampling through SNR, tracking, penetration, and retrieval bias?
(2) Under what conditions do commercial and partner-mission observations provide usable and complementary information for global and regional NWP?
(3) What additional consistency, uncertainty, and stewardship requirements apply to the use of multi-mission RO observations for environmental monitoring and climate records?

In this review, we use the evaluation framework in Figure 2 to compare the performance of commercial RO data with that from national missions. Figure 2 provides a diagnostic structure for organizing the reviewed evidence. Physically motivated dependencies guide the evaluation, but the available comparisons generally do not isolate the contributions of instrument characteristics, atmospheric state, sampling, and processing. Dashed arrows indicate influences of atmospheric state and processing choices at multiple stages. In this paper, we used this framework, with signal quality, retrieval quality and uncertainty, sampling complementarity, and application-specific value as diagnostic pathways.

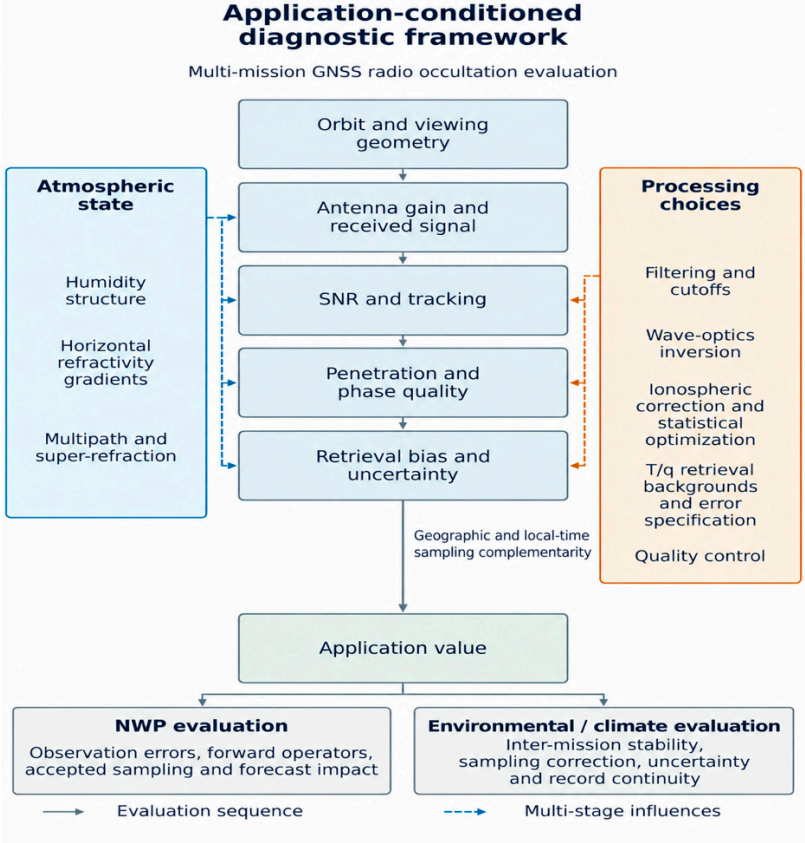


Figure 2. Application-conditioned diagnostic framework for evaluating multi-mission GNSS radio occultation (RO) observations. Dashed arrows indicate influences of atmospheric state and processing choices at multiple stages. Arrows organize diagnostic relationships and evaluation steps; they do not establish causal attribution.

Previous studies have addressed individual components of the evaluation framework. For example, commercial-mission evaluations indicate that SNR, receiver characteristics, occultation geometry, atmospheric conditions, and processing choices jointly affect penetration and retrieval statistics, although their individual contributions are rarely isolated [8,10–15]. Data-assimilation experiments also show that commercial observations can improve global and regional forecasts when the observations pass quality control, complement the existing observing system, and are assigned appropriate observation errors and forward operators [16–20]. For environmental monitoring and climate applications, however, short-term retrieval agreement alone is insufficient. These applications also require common processing, inter-mission overlap, sampling correction, structural-uncertainty characterization, version control, and sustained data stewardship [4,21–23]. Thus, the literature provides substantial evidence for individual links in the observing chain but does not yet provide a unified, cross-mission basis for consistently addressing all three questions above.

NOAA/NESDIS established a GNSS RO program at the Center for Satellite Applications and Research (STAR) around 2018 to support operational processing, global environmental monitoring, and NWP. STAR has used this evaluation pathway to examine the measurement characteristics and retrieval quality of COSMIC-2 and other RO missions [9,24,25]. STAR also evaluated their impact on Atlantic hurricane forecasts [17,25]. We also developed independent capabilities for excess-phase-to-bending-angle and refractivity processing and one-dimensional variational retrievals [9,15]. These activities provide NOAA/STAR with a basis for examining the three questions above for commercial GNSS RO data.

This article is a selective narrative review, not a systematic review. It synthesizes peer-reviewed studies together with clearly identified operational, technical, and conference evidence available through August 2026. In this study, we emphasize neutral-atmosphere observations evaluated or processed by NOAA/STAR, along with complementary results from other centers. We interpret each line of evidence according to the quantity evaluated: signal characteristics, retrieval quality, quality-controlled usable yield, sampling complementarity, or application impact. Conclusions are restricted to the reported missions, periods, processing chains, and applications.

Our review is organized into four linked evaluation levels: (1) mission and signal characteristics; (2) retrieval quality and uncertainty; (3) spatiotemporal sampling complementarity; and (4) application-specific value. Level 4 branches into operational NWP and environmental or climate applications because these uses require different evidentiary standards. Section 2 reviews observation characteristics from mission design through retrieval uncertainty. Section 3 assesses global NWP and tropical-cyclone applications; Bai et al. [26] provide complementary context in their recent review of tropical-cyclone assimilation. Section 4 examines environmental and climate applications. Section 5 identifies remaining challenges and testable priorities, and Section 6 presents the conclusions.

2. Review of Observation Characteristics: From Mission Design to Retrieval Uncertainty

In this section, we reviewed commercial RO data characteristics (the first 5 rectangles of Figure 2) and compared them with those from national missions. Section 2.1 discusses mission coverage, antenna design, viewing geometry, and SNR (rectangles 1–3). Section 2.2 addresses penetration and precision (rectangles 4–5), and Section 2.3 examines the relationship between SNR and lower-tropospheric retrievals. We detailed the NWP and climate applications in Sections 3 and 4, respectively.

2.1. Mission Coverage, Antenna Design, and Viewing Geometry

2.1.1. Global and Local-Time Coverage

Mission orbits determine the spatial and temporal coverage of RO observations. Except for COSMIC-2, Spire, PlanetiQ, and most other RO missions use sun-synchronous orbits that sample specific local times. Figure 3 shows the spatial and hourly local-time distributions of RO sample counts in 5° latitude bins for Spire, COSMIC-2, and PlanetiQ, where both Spire and COSMIC-2 data are from 8 September 2021 to 15 March 2022, and PlanetiQ data are from 1 September 2022 to 30 November 2022.

Because most Spire and PlanetiQ satellites operate at high inclinations, these two missions, together with MetOp, provide coverage from nearly 90°N to 90°S. Spire observations mainly cover 02–03, 09–10, 14–15, and 21–22 local time, whereas PlanetiQ observations cover 01–04, 09–10, and 21–22 local time.

Unlike PlanetiQ and Spire, the six-satellite COSMIC-2 constellation has an inclination of approximately 24° and samples most local times in the tropics and midlatitudes. Each COSMIC-2 satellite has one forward-looking and one backward-looking antenna, with viewing directions of 0° and 180°, respectively, relative to the flight direction. Consequently, COSMIC-2 observations outside 24°N–24°S are collected at larger antenna azimuth angles, which are associated with lower SNR, as discussed below. COSMIC-2 observations are concentrated between 45°N and 45°S, and more than 70% occur within 24°N–24°S.

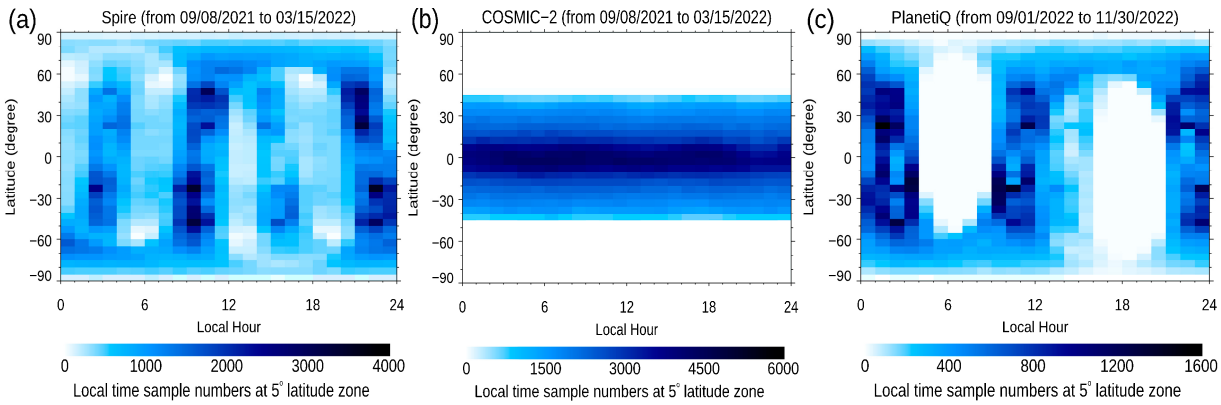


Figure 3. Spatial and hourly local-time distributions of RO sample counts in 5° latitude bins for (**a**) Spire, (**b**) COSMIC-2, and (**c**) PlanetiQ. The color bar indicates the number of observations in each 5° latitude bin.

2.1.2. SNR Distribution and Its Relationship to Viewing Geometry

Here, SNR is defined as the magnitude of the RO signal divided by the receiver noise level and is expressed in voltage-to-voltage units (V/V). The magnitude and distribution of SNR depend on GNSS transmitter power, receiver intermediate-frequency bandwidth, RO antenna design and gain pattern, viewing geometry, and occultation azimuth relative to true north [8]. These mission- and processing-dependent factors must be considered when comparing SNR distributions.

Consistent with its larger antenna and higher gain, Figure 4 shows that COSMIC-2 L1 SNR is approximately 2–3 times that of Spire. In this comparison, PlanetiQ SNR is comparable to COSMIC-2 SNR. Note that Figure 4 only shows the relative magnitude of the SNR distributions among missions and is not calculated in the same 1 Hz noise bandwidth. Gorbunov et al. [27] provided comparisons using both mission–GNSS-specific modal noise floors and event-specific noise-floor estimates. Their published GPS results give median statically normalized SNRs of 74.7 V/V for COSMIC-2 and 31.6 V/V for Spire (see Tables 3 and 4 in reference [27]), corresponding to a ratio of approximately 2.36. The normalized SNRs for Metop-A, -B, and -C range from 55.4 V/V to 66.7 V/V, which is compatible with that of COSMIC-2. PlanetiQ GPS L1 noise-floor-normalized SNR results were not available in Gorbunov et al. [27].

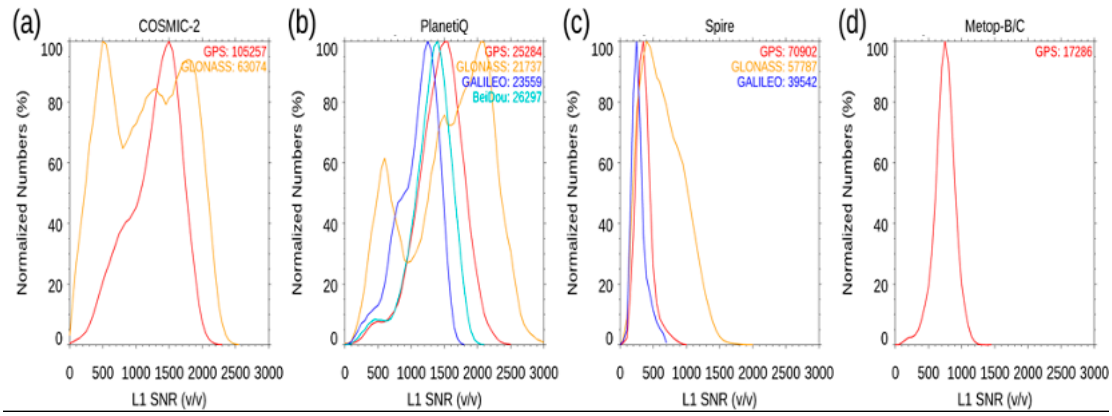


Figure 4. Normalized SNR sample-frequency distributions (the number of samples in each SNR bin divided by the maximum number among all SNR bins) for Global Positioning System (GPS; red

line), Globalnaya Navigatsionnaya Sputnikovaya Sistema (GLONASS; orange line), Galileo (blue line), and BeiDou (green line) for (**a**) COSMIC-2, (**b**) PlanetiQ, (**c**) Spire, and (**d**) MetOp-B/-C during 1–30 September 2022.

Table 2 shows that COSMIC-2 and PlanetiQ use higher signal sampling rates than Spire and MetOp. COSMIC-2 and PlanetiQ generally sample at 100 Hz, whereas Spire and MetOp sample at 50 Hz; PlanetiQ Galileo data are sampled at 125 Hz. However, signal sampling rate alone does not determine the atmospheric structure resolved in a retrieved profile; receiver bandwidth, tracking, smoothing, wave-optics processing, and vertical sampling also contribute. Table 2 summarizes the receivers, RO antennas, tracked GNSS constellations, signal sampling rates, and Precise Orbit Determination (POD) antenna characteristics for the missions examined.

Table 2. Receivers, RO antenna types, tracked GNSS constellations, signal sampling rates, and POD antenna characteristics for COSMIC-2, Spire, MetOp-B, MetOp-C, and PlanetiQ. G: GPS; R: GLONASS; E: Galileo; C: Beidou; E*: available after 25 September 2024.

	Spire (>20)	**PlanetiQ**	**COSMIC-2 (6)**	**MetOp-B/-C**
Receiver	STRATOS	PYXIS	TGRS	GRAS
RO Antenna	2/G, R, E (50 Hz)	2/G, R, E, C (G/R/C: 100 Hz; E: 125 Hz)	2/G, R, E* (100 Hz)	2/G (50 Hz)
POD Antenna	1/G, 1 Hz/50 Hz	2/G, R, 1 Hz	2/G, R, 1 Hz only	1/G, 1 Hz

Although COSMIC-2 has a higher mean SNR than Spire, its SNR distribution depends strongly on viewing geometry. Unlike nadir-viewing infrared and microwave sounders, GNSS RO missions observe limb signals through dedicated forward- and backward-looking antennas (i.e., COSMIC-2) and sideward-looking antennas (i.e., Spire and PlanetiQ). COSMIC-2 uses a 3 × 4 phased-array helical antenna design to enhance tropical SNR coverage [28]. Each COSMIC-2 flight module carries two TGRS RO antennas, one forward-looking (+X) and one backward-looking (−X). The effective RO viewing angles (also see Chen et al. [24]), measured relative to the spacecraft's orbital velocity vector, are approximately 23–66° and 115–158°, respectively. Under this convention, 0° denotes forward viewing and 180° denotes backward viewing. The sample distributions peak near 24° and 157°, respectively.

The latitudinal distribution of COSMIC-2 SNR is closely associated with its antenna viewing geometry. Figure 5a,b shows the COSMIC-2 antenna zenith angle and corresponding SNR. Given its low inclination, COSMIC-2 has the highest mean SNR near 24°N and 24°S. Mean SNR decreases toward the equator and the outer limits of the latitude coverage as antenna zenith angle increases. For the distributions shown, antenna zenith angle is strongly negatively correlated with SNR, with correlation coefficients of −0.97, −0.92, −0.91, −0.91, and −0.94 for 30°S–45°S, 10°S–30°S, 10°N–10°S, 30°N–10°N, and 45°N–30°N, respectively. The correlation coefficients are directly calculated from individual samples shown in Figure 5a,b but separated at each latitude zone. Figure 5c,d show the corresponding Spire antenna zenith angle and SNR distributions. These correlations provide strong evidence of an observed association between viewing geometry and SNR.

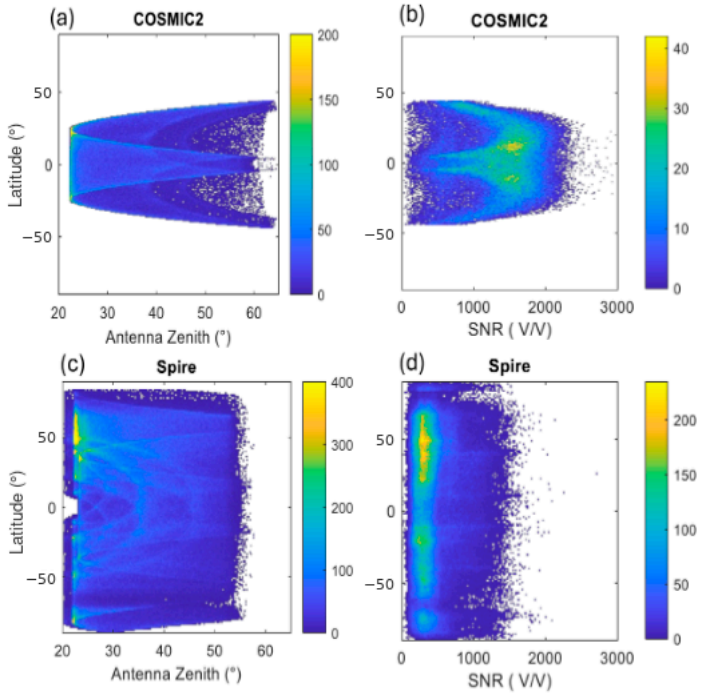


Figure 5. Latitudinal distributions of (**a**) antenna zenith angle and (**b**) SNR for COSMIC-2, and (**c**) antenna zenith angle and (**d**) SNR for Spire.

2.2. Penetration Depth, Precision, and Uncertainty Among Missions

2.2.1. Relationship Between SNR and RO Penetration Depth

Penetration depth is also an indicator of GNSS RO data quality [6,8,29]. The cited studies indicate that, across missions, antenna design and viewing geometry influence the magnitude and distribution of SNR, which in turn are associated with RO penetration and data quality. COSMIC-2 SNR is lower in the midlatitudes and higher in 30°N–10°N and 10°S–30°S (Figure 5b), whereas the Spire SNR distribution is more spatially uniform (Figure 5d). Schreiner et al. [29] and Ho et al. [6,8] found that the lowest RO tracking penetration height is usually associated with SNR and atmospheric dryness. Figure 6a–c show the lowest monthly mean penetration height in each 5° × 5° grid for COSMIC-2, Spire, and PlanetiQ. Because the RO ray may be blocked by mountains over land, we show the penetration depth over oceans only. To be consistent, we used UCAR CDAAC-processed COSMIC-2, Spire, and PlanetiQ data. Table 3 summarizes the lowest penetration height corresponding to 80% of the total profiles for each mission and latitude zone.

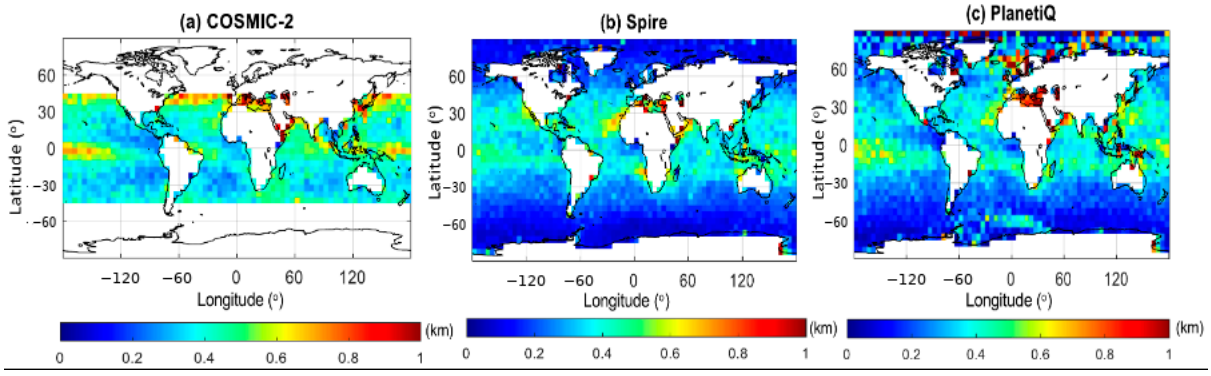


Figure 6. Global distributions of monthly mean lowest penetration height for 80% of total RO profiles during October–November 2022, binned on a 5° × 5° grid, for (**a**) COSMIC-2 (45°S–45°N), (**b**) Spire, and (**c**) PlanetiQ.

Figure 6 indicates that RO observations generally penetrate deeper in drier atmospheres and that the relationship between SNR (see Figure 5) and penetration varies with latitude and mission. COSMIC-2 penetrates slightly lower than Spire in some subtropical zones (see Table 3). COSMIC-2 SNR is lower in the midlatitudes and higher in 30°N–10°N and 10°S–30°S (Figure 5b), whereas the Spire SNR distribution is more spatially uniform (Figure 5d). At tropical latitudes and near the outer limits of COSMIC-2 coverage, however, Spire and PlanetiQ penetrate lower than COSMIC-2, consistent with the latitude-dependent COSMIC-2 SNR distribution. Accordingly, higher mission-mean SNR does not ensure uniformly deeper penetration at all latitudes.

Table 3. Lowest penetration heights (km) corresponding to 80% of the total profile for different RO missions and latitude zones (see [6]). An em dash indicates that COSMIC-2 did not provide coverage in the corresponding latitude band for this comparison. This table is also for October–November 2022.

	10°N–10°S	30°N–10°N	10°S–30°S	45°N–30°N	30°S–45°S	60°N–45°N	45°S–60°S	90°N–60°N	60°S–90°S
COSMIC-2	0.79	0.64	0.54	0.99	0.60	—	—	—	—
Spire	0.64	0.71	0.55	0.58	0.35	0.38	0.22	0.18	0.11
PlanetiQ	0.72	0.73	0.61	0.59	0.36	0.38	0.22	0.24	0.10

2.2.2. Precision in the Neutral Atmosphere Among RO Missions

Several studies [6,8,24] used coplanar profile pairs from the same mission but different receivers to assess whether higher SNR is associated with improved RO precision from the surface to the UTLS (upper troposphere and lower stratosphere). RO-RO coplanar pairs for the same missions with a time window of less than 20 min and a distance of less than 200 km between RO event positions are collected. The standard deviation of COSMIC-2 coplanar pairs is larger than that of COSMIC-1–COSMIC-1 and Spire–Spire pairs (Figure 7c) over 45°N–20°N (Figure 7c), and 20°S–45°S (Figure 7a), especially in the lower troposphere at 20°S–45°S and 45°N–20°N. This may be owing to the relatively lower SNR for COSMIC-2 in those regions (see Figure 5b). Note that these data are all processed by CDAAC (COSMIC Data Analysis and Archive Center).

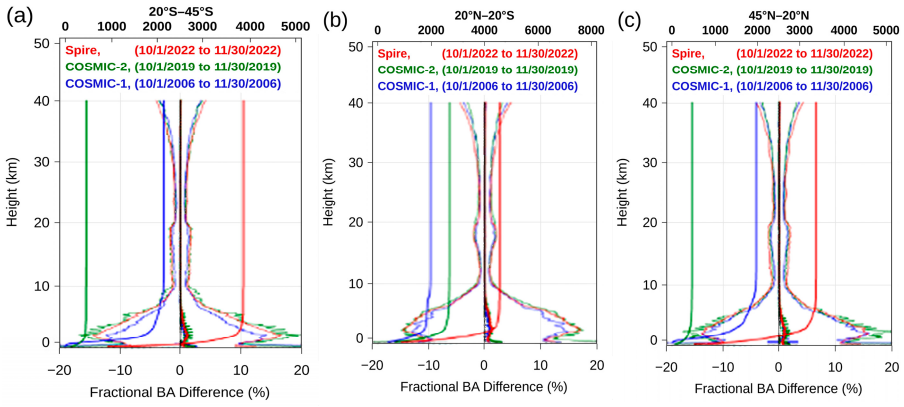


Figure 7. Fractional BA difference, corresponding standard deviation, and sample count from the surface to 40 km for Spire (red lines), COSMIC-2 (green lines), and COSMIC-1 (blue lines) at (**a**)

20°S–45°S, (**b**) 20°N–20°S, and (**c**) 45°N–20°N. The standard error of the mean (SEM) is shown as a horizontal line superimposed on the mean differences.

In the UTLS and above 25 km, however, the higher-SNR COSMIC-2 observations have slightly smaller coplanar-pair standard deviations than COSMIC-1 and Spire. Available studies indicate that although Spire has lower SNR than COSMIC-2, its penetration, precision, accuracy, and uncertainty are comparable to those of higher-SNR missions, including COSMIC-2 and PlanetiQ [8,30,31].

2.3. Relationship Between Higher SNR and Lower-Tropospheric Retrievals

To examine the relationship between SNR and COSMIC-2 retrievals, using COSMIC-2 data from 6 October 2025, we generated stratified figures for (a) 20°S–45°S, (b) 20°N–20°S, and (c) 45°N–20°N (see Figure 8). The results show larger biases in the moist tropics than at midlatitudes. However, we did not find that higher SNR eliminates the negative biases either over the drier hemisphere or the tropics (see more discussion below).

Several studies [8,31] indicate that Spire and PlanetiQ retrievals are broadly consistent with COSMIC-2. Figure 9 shows PlanetiQ fractional bending-angle departures from ERA5 for different latitude zones. Note that for the NOAA RODB-2 DO-4 delivery covering 18 September 2024–18 September 2025, PlanetiQ added artificial random noise to its observations before delivery to NOAA, yielding an average SNR of approximately 400 V/V at straight-line heights of 60–80 km (personal communication). The PlanetiQ SNRs in Figure 9 are all close to 400 V/V. PlanetiQ's accuracy is comparable to that of COSMIC-2, although Figures 8 and 9 use different latitude zones. The RO-ERA5 comparisons are consistent with those of RO-RAOB comparisons and are not further discussed (Ho et al. [6,8]).

Note that SNR is a useful indicator of signal tracking and penetration, especially when interpreted together with atmospheric dryness and viewing geometry. However, higher SNR alone does not resolve water-vapor variability along the ray path, departures from spherical symmetry, turbulence, multipath, and processing-related effects. Consequently, higher-SNR observations do not necessarily have smaller lower-tropospheric retrieval biases or uncertainties [7,8,32].

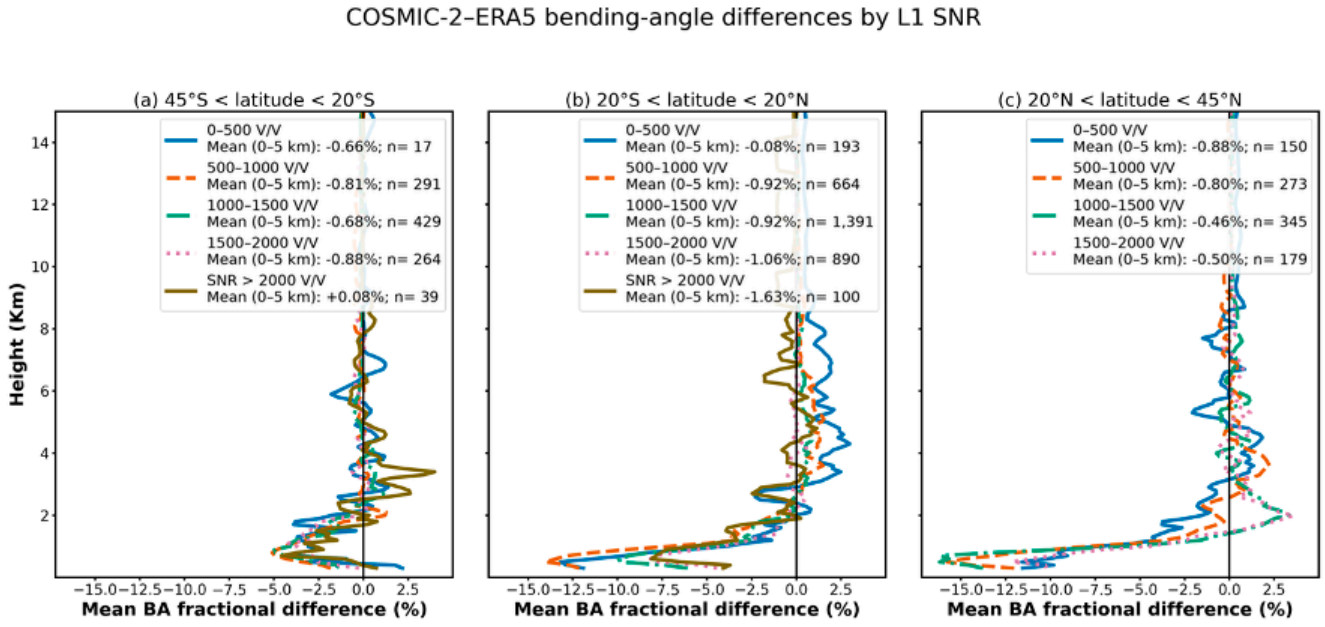


Figure 8. COSMIC-2 fractional bending-angle departures from ERA5 (defined as 100% × (COSMIC-2 − ERA5)/ERA5) for different L1 SNR groups and heights above mean sea level for (**a**) 20°S–45°S, (**b**) 20°N–20°S, and (**c**) 45°N–20°N. The mean fractional bending-angle departures from ERA5 are calculated from the surface to 5 km.

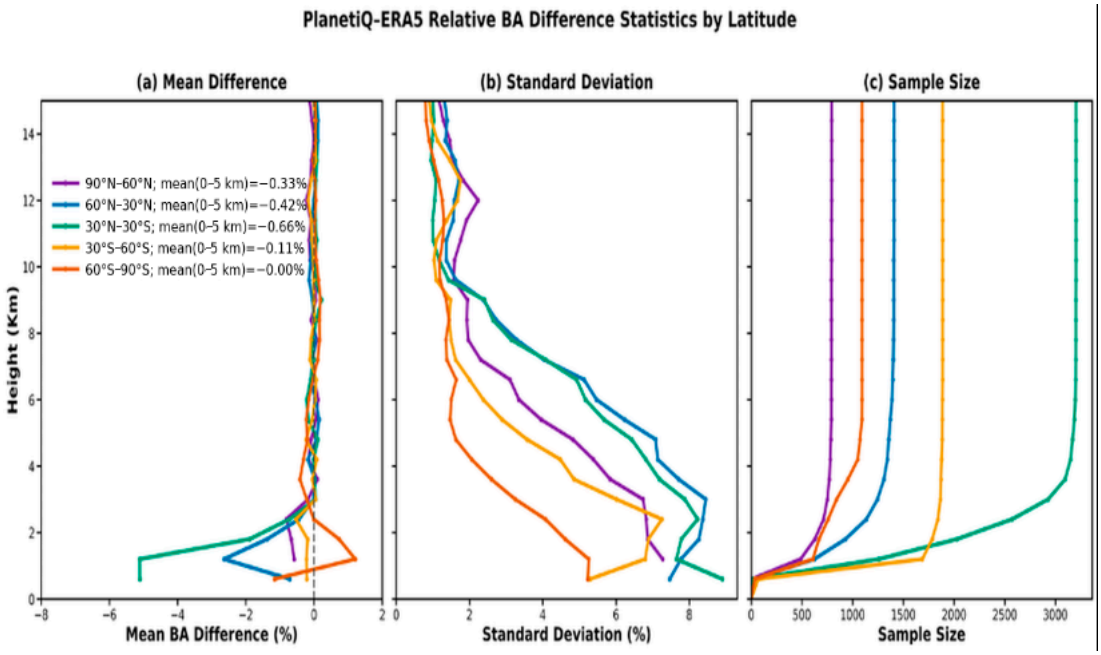


Figure 9. PlanetiQ fractional bending-angle departures from ERA5 for different latitude zones for (**a**) Mean difference (%), (**b**) Standard deviation (%), and (**c**) the sample size for 90°N–60°N, 60°N–30°N, 30°N–30°S, 30°S–60°S, and 60°S–90°S.

In summary, the comparisons reviewed in Section 2 show that higher SNR generally improves tracking and lower-tropospheric penetration, but does not by itself remove biases and uncertainties from atmospheric conditions such as water-vapor irregularity, multipath tracking, and super-refraction. Spire and PlanetiQ retrievals are broadly compatible with COSMIC-2 and partner missions in the principal atmospheric layers. In addition, antenna gain and viewing geometry affect SNR, supporting signal tracking and penetration. However, transmitter power, receiver bandwidth, atmospheric moisture structure, and ray-path geometry also play a role.

3. Review of Commercial RO Applications in Weather Forecasting

This section reviews the effects of assimilating commercial RO observations using three complementary results: Forecast Sensitivity to Observation Impact (FSOI), observing-system experiments (OSEs), and regional tropical-cyclone studies. It also summarizes results obtained using the Ensemble of Data Assimilations approach [30,33]. Because Spire observations have been evaluated over a longer period than PlanetiQ observations, the published evidence reviewed here is weighted toward Spire.

3.1. Commercial RO Data Assimilation Impacts on Global NWP

3.1.1. Forecast Sensitivity to Observation Impact Studies

Although Spire uses a smaller antenna and generally has lower SNR than COSMIC-2, its bending-angle accuracy is broadly comparable in the principal assimilation layers [8]. Forecast Sensitivity to Observation Impact (FSOI) is an adjoint-based diagnostic that quantifies the contribution of assimilated observations to a 24 h forecast-error metric [34–36]. In the ECMWF system, the relative FSOI contribution of GNSS RO increased after

COSMIC-2 was assimilated and increased further after approximately 5000 Spire profiles per day were added (Figure 10; see [30]). FSOI percentages depend on the observing system, evaluation period, forecast-error norm, data volume, and normalization. Therefore, the results indicate the incremental value of additional RO coverage rather than establishing a universal ranking of observation types.

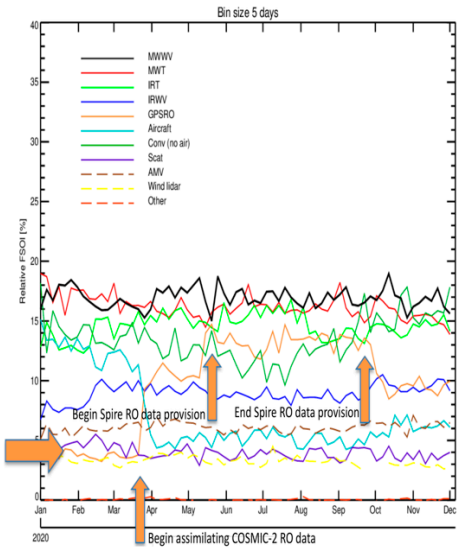


Figure 10. Time series of relative Forecast Sensitivity to Observation Impact (FSOI; %) for different observation categories in the ECMWF forecasting system during January–December 2020, shown in 5-day bins. Legend entries denote satellite microwave radiances sensitive to water vapor, clouds, and precipitation (MWWV; black line); microwave temperature-sounding radiances (MWT; red line); infrared temperature-sounding radiances (IRT; light green line); infrared water-vapor-sounding radiances (IRWV); GNSS RO bending angles (solid green line); aircraft meteorological observations (Aircraft); conventional observations excluding aircraft, including radiosonde and surface observations [Conv (no air)]; scatterometer ocean-surface winds (Scat); satellite-derived atmospheric motion vectors (AMV); Aeolus Doppler wind-lidar observations (Wind lidar); and remaining observation types grouped in the source dataset (Other). Arrows indicate the start of COSMIC-2 assimilation and the beginning and end of the indicated Spire RO data-provision period. (Source: Sean Healy, ECMWF).

3.1.2. Observing System Experiments Evaluating RO Data

Global NWP centers began assimilating COSMIC-2 data in late 2019 and early 2020 [37,38]. Many studies have used OSEs to assess the impact of assimilated RO data on global weather forecasts by comparing forecast errors across cycled DA experiments that turn assimilation of selected observation datasets on and off. For example, NCEP reported that quality controls (QCs) in its global NWP model reject most RO data below 700–800 hPa. Evaluations of NCEP's current Global Forecast System (GFS) indicate that assimilating COSMIC-2 primarily affects the upper troposphere and lower stratosphere, consistent with earlier findings for COSMIC-1.

Several global operational centers conducted DA experiments to assess whether Spire RO data provide information beyond other RO missions and improve NWP. Bowler [16] evaluated innovation statistics and forecast impacts from Spire GNSS RO bending angles assimilated in the UK Met Office (UKMET) global model from September to December 2019. The Control run assimilated operational RO bending angles, mostly from MetOp; COSMIC-2 assimilation had not yet been implemented. The Spire experiment assimilated a dataset approximately 2.5 times larger than the MetOp dataset. The

experiment produced statistically significant root-mean-square-deviation (RMSD) reductions relative to ECMWF analyses for most forecast times, meteorological fields, and height layers evaluated in the Northern Hemisphere, Southern Hemisphere, and tropics. Bowler [16] also varied the number of assimilated Spire observations and found that the overall forecast RMSD reduction across a range of variables, verified against both ECMWF analyses and observations, was roughly proportional to the logarithm of the total number of assimilated GNSS RO observations. This result is consistent with Harnisch et al. [39].

Lonitz et al. [33] evaluated the effects of assimilating COSMIC-2 bending angles, with and without additional Spire RO data, on ECMWF and UKMET global forecasts from 1 January to 31 March 2020. COSMIC-2 DA improved ECMWF and UKMET forecasts of temperature, humidity, and wind. In these experiments, adding Spire observations to COSMIC-2 further improved these fields in certain regions. Substantial improvements occurred in upper-tropospheric temperature, where RO data have the lowest uncertainty [40]. For example, assimilating COSMIC-2 and Spire observations improved UKMET forecast-temperature fits to tropical radiosondes by approximately 15% relative to a Control that withheld both observation sets.

Together, these studies indicate that commercial Spire observations can improve global and regional NWP when they supplement other assimilated RO missions. The magnitude of the benefit depends on the number and distribution of assimilated profiles, quality control, observation-error specification, forward operator, model system, verification reference, region, and forecast variable. Thus, the results support the incremental value of additional commercial RO observations rather than a universal ranking of missions.

3.2. Impacts of Spire and ROMEX Data Assimilation on Tropical-Cyclone Forecasts

Tropical cyclone (TC) genesis and intensification can be strongly sensitive to lower- to mid-tropospheric water vapor near the storm [41–44]. With their all-sky observability and fine vertical resolution—typically sub-kilometer but dependent on variable altitude sampling and retrieval processing—GNSS RO profiles can provide useful water-vapor information for NWP model TC forecasts [1,3,45]. Teng et al. [46] compared WRF forecasts of 32 western North Pacific TC precursor disturbances from 2019, initialized after 72 h of cycled DA in two configurations: "GTS," which assimilated only conventional observations, and "EPH," which also assimilated GNSS RO refractivity, mostly from COSMIC-2, using a nonlocal forward operator. In these experiments, Teng et al. [46] reported that cycled RO DA improved TC cyclogenesis detection in WRF, as measured by a 19% increase in the accuracy rate and a 20% reduction in the false alarm ratio.

Compared with GTS, EPH produced stronger lower-tropospheric cyclonic vorticity for developing cases and weaker vorticity for non-developing cases (Figure 11a,b). These differences are consistent with the interpretation that the water vapor and temperature information from COSMIC-2 RO observations assimilated in EPH improved WRF's low-level wind representation through dynamical coupling during the 72 h cycled DA spin-up. Chen et al. [47] showed a similar result when evaluating COSMIC-1 observation assimilation in a regional model. Consistent with previous COSMIC-1 DA impact studies [44,47,48], COSMIC-2 assimilation also increased water vapor in a deep layer near developing TC disturbances in the WRF initial conditions and forecasts (Figure 11c).

Furthermore, compared to developing TCs, COSMIC-2 assimilation yields a substantially smaller and less persistent mid-tropospheric water vapor increase within circulations surrounding non-developing TC disturbances (Figure 11c,d). This is consistent with our understanding that positive feedback mechanisms between inner-core convective organization, wind fields, and tropospheric water vapor can exist for developing TCs. For example, increasingly intense and well-organized inner-core deep

moist convection can help drive humidification of the troposphere by strengthening the convergence of moist airflows directed toward the inner-core convection (Charney and Eliassen [49]). Additionally, strengthening near-surface winds can increase ocean-to-air latent heat fluxes, causing amplification of a TC's "in-up-out" secondary circulation and increased humidity throughout the inner-core troposphere (Emanuel [50]).

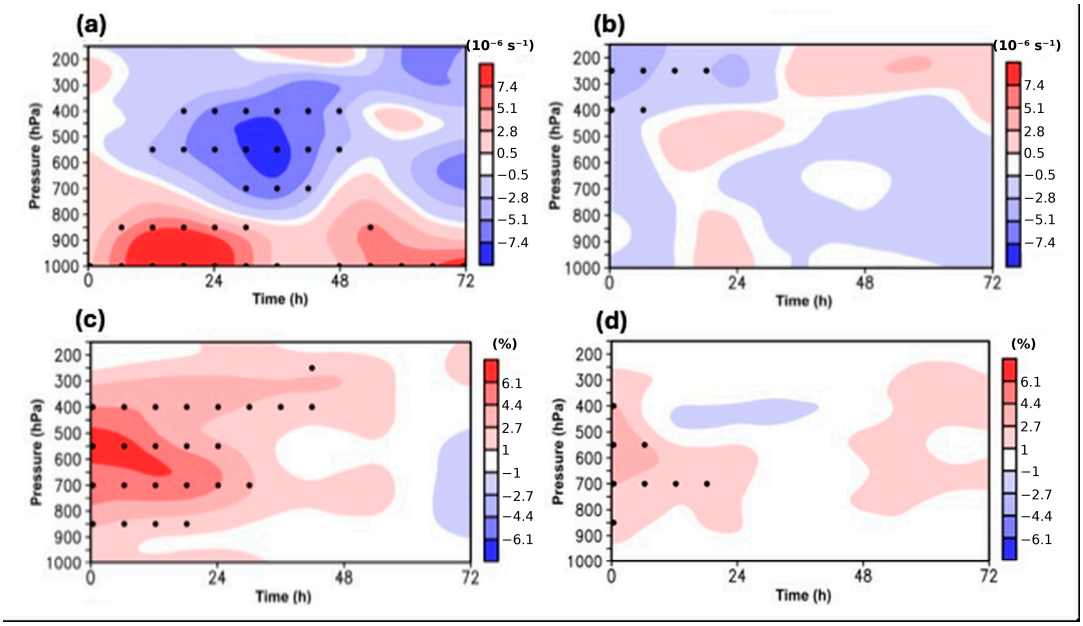


Figure 11. (**a**,**b**) Time–height cross-sections of EPH–GTS differences in relative vorticity averaged within a 5° radius of the tropical-disturbance center, for WRF forecast composites from (**a**) the 9 developing TC cases and (**b**) the 23 non-developing cases. (**c**,**d**) As in (**a**,**b**) but for relative humidity. Dots denote differences significant at the 90% confidence level using the *t*-test [46].

Miller et al. [17] conducted data-denial experiments using four 2022 Atlantic hurricanes to evaluate the impact of assimilating Spire bending angle data in HWRF. The Control forecasts withheld COSMIC-2 and Spire, whereas the C2 and C2Spire experiments added COSMIC-2 alone and COSMIC-2 plus Spire, respectively. Although COSMIC-2 assimilation helped reduce Control's minimum central sea-level pressure (P_{MIN}) over-intensification bias in medium-to-long range forecasts, adding the Spire data led to a more substantial ~15–35% P_{MIN} bias improvement (Figure 12). Short-range C2Spire temperature and specific-humidity RMSDs against dropsondes were 5–10% smaller compared to Control. These results indicate a beneficial incremental Spire impact for the cases examined, although the four-storm sample limits broader generalization.

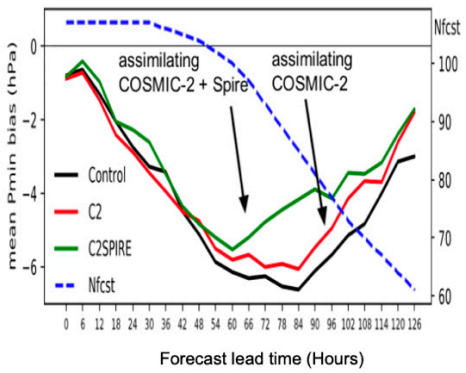


Figure 12. Time series of the mean HWRF P_{MIN} bias (hPa) relative to the National Hurricane Center's best-track data for Control (black line), C2 (red line), and C2Spire (green line). The dashed blue line indicates the number of forecasts used to compute the mean. The *x*-axis is forecast lead time (hours).

Miller et al. [20] evaluated the impact of assimilating EUMETSAT-processed commercial GNSS RO bending-angle observations in Hurricane Analysis and Forecasting System (HAFS) forecasts of four 2022 Atlantic hurricanes. Their study supported the multi-center Radio Occultation Modeling Experiment (ROMEX) [30], which investigated the effects of assimilating a large commercial RO observation dataset on forecasts from major operational centers worldwide. The ROMEX dataset included approximately 17,000 Spire and 3000 PlanetiQ RO bending angles per day globally. Miller et al. [20] found that, compared with a Control that assimilated COSMIC-2 and other operational RO platforms, a ROMEX configuration that additionally assimilated Spire and PlanetiQ reduced average TC P_{MIN} intensity errors by about 10% during the first 30 forecast hours. The ROMEX-assimilating experiment also produced a statistically significant reduction in HAFS medium-range forecast specific-humidity RMSD relative to ERA5 in the 900–500 hPa layer at around 42 to 60 h and in the 1000–400 hPa layer around 78 to 84 h (Figure 13).

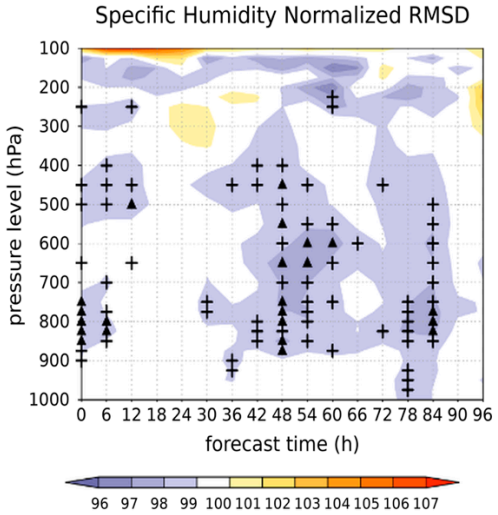


Figure 13. Time–height plot of the HAFS forecast specific-humidity RMSD percentage ratio relative to ERA5, defined as 100 × RMSD_ROMEX/RMSD_Control, where ROMEX assimilated Spire and PlanetiQ in addition to the observations in Control. Crosses and triangles denote statistically significant RMSD differences at the 95% and 99% confidence levels, respectively. Eighty-four HAFS forecasts were used for verification.

3.3. Observation-Error Estimates and Lower-Tropospheric Use

The effective use of observations in data assimilation depends on an appropriate observation-error matrix, which controls the relative weighting of observations and the model background. For RO bending angles, the effective error includes instrument and retrieval uncertainty, forward-operator error, atmospheric representativeness, and reference or background error. These components vary with altitude, atmospheric water-vapor structure, viewing geometry, processing, and NWP-model resolution.

Recent approaches estimate profile- or regime-dependent RO uncertainty from observation and environmental diagnostics and use bending-angle uncertainty to support more adaptive quality control and error weighting [51,52].

Figure 14a shows the altitude-dependent bending-angle observation errors used by ECMWF. Expressing the error as a percentage of observed bending angle yields larger

specified absolute errors in the moist lower troposphere, where bending angles are larger. However, this specification does not explicitly represent horizontal water-vapor gradients or mission-dependent retrieval uncertainty. Figure 14b,c show COSMIC-2 bending-angle uncertainty estimated with the three-cornered-hat method using ERA5 and MERRA-2 as comparison datasets [53–55]. The diagnosed uncertainty is larger in latitude bands with greater lower-tropospheric water-vapor inhomogeneity. These estimates combine observation, comparison-data, and representativeness effects and depend on the assumptions of the three-cornered-hat method. More complete observation-error models should account for atmospheric structure, retrieval uncertainty, vertical error correlation, and forward-operator limitations.

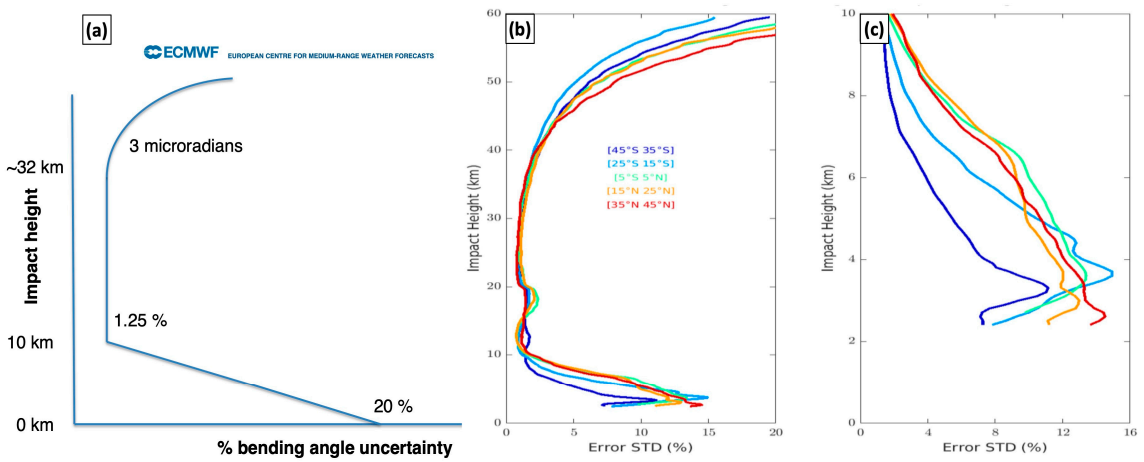


Figure 14. (**a**) Bending-angle observation-error profile used for all GNSS RO platforms assimilated by ECMWF, specified relative to the observed bending angle below approximately 32 km, with an absolute error of 3 μrad above that height. (**b**) COSMIC-2 bending-angle error standard-deviation profiles estimated with the three-cornered-hat (3CH) method for August 2021 and stratified into 10° latitude bands. The 3CH calculations compared COSMIC-2 observations with bending angles computed using a one-dimensional forward operator from refractivity derived from ERA5 short-term forecasts and NASA's Modern-Era Retrospective Analysis for Research and Applications version 2 (MERRA-2) 6 h-old analyses as comparison datasets. (**c**) Same as (**b**), enlarged for the 0–10 km impact-height layer. (**a**) Image courtesy of ECMWF. (**b**,**c**) From Anthes et al. [54].

In summary, the reviewed FSOI, global OSE, and regional tropical cyclone DA impact experiment results consistently indicate that additional commercial RO profiles can provide incremental forecast value. The OSE impact depends on accepted profile volume, geographic and local-time distribution, quality control, and observation-error specification. The lower troposphere remains one of the most challenging areas among GNSS RO applications.

4. Review of Environmental and Climate Applications

Consistently processed products from multiple RO missions available since 2006 support nearly two decades of environmental monitoring. Section 4.1 summarizes atmospheric applications, whereas Sections 4.2–4.4 review the distinct consistency requirements for UTLS temperature, tropospheric water-vapor variability and trends, and planetary-boundary-layer height records.

4.1. Detecting Atmospheric Variations Using RO Data

GNSS RO provides high-resolution, all-weather observations of the neutral atmosphere and is well suited to detecting vertically localized atmospheric variations

[1,3]. The literature reviewed by Ho et al. [7] and Bonafoni et al. [56] includes gravity waves, tropical tides, cloud-related structures, extreme events, and UTLS temperature perturbations. These studies illustrate the value of RO as a vertically resolved complement to passive infrared and microwave observations rather than as a replacement.

With improved spatial and temporal coverage from recently available RO missions (Figures 1 and 3), Babu and Liou [57] demonstrated that RO profiles can detect UTLS temperature anomalies caused by volcanic eruptions. By combining Microwave Limb Sounder (MLS) water-vapor measurements with collocated RO data, Randel et al. [58] identified water-vapor overshooting into the UTLS due to a volcanic eruption. These studies indicate that combining RO data with infrared and microwave satellite measurements can provide atmospheric information not available from the individual datasets.

4.2. Construction of a UTLS Temperature Environmental Data Record from Consistently Processed Multi-Mission RO Data

Many studies have assessed the consistency and long-term stability of RO observations and indicate that RO records can be used to estimate climate trends in the UTLS [3,4,7,59–61]. GNSS RO has also been widely used to estimate upper-air temperature trends, with evaluations against infrared and microwave soundings and several model systems [62–68]. A long-term monthly zonal-mean record is important for climate monitoring and intercomparison among data sources.

Several RO processing centers have applied consistent processing to construct long-term RO climatologies. For example, the RO Meteorology Satellite Application Facility (ROM SAF) generated a multi-mission environmental data record from MetOp, COSMIC-1, CHAMP, and GRACE, covering 2001–2016 [66]. Additionally, the STAR GNSS RO Science Data Center (SDC, https://gpsmet.umd.edu/gnssro/index.php (accessed on 5 November 2026)) has used a reconfigured ROPP (STAR ROPP; see STAR-ROPP ATBD V1.0 at https://gpsmet.umd.edu/star_gnssro/img/ATBD_STAR_ROPP_final.pdf (accessed on 5 November 2024)) to process data from multiple RO missions since 2006. These products were validated against results from the STAR Full Spectrum Inversion (FSI) algorithm [15]. Using consistently processed RO data, the STAR SDC developed a UTLS temperature environmental data record spanning September 2006–July 2023 [22].

Before combining RO missions into an environmental data record, their consistency and long-term stability must be assessed. Figure 15 compares collocated COSMIC-1, COSMIC-2, and Spire temperatures with MetOp-A/-B/-C in the 20–30 km layer [22]. MetOp has the longest common mission record in this comparison and is used as the reference. The median and central 68% range characterize the differences. This comparison assesses inter-mission consistency and does not treat MetOp as error-free.

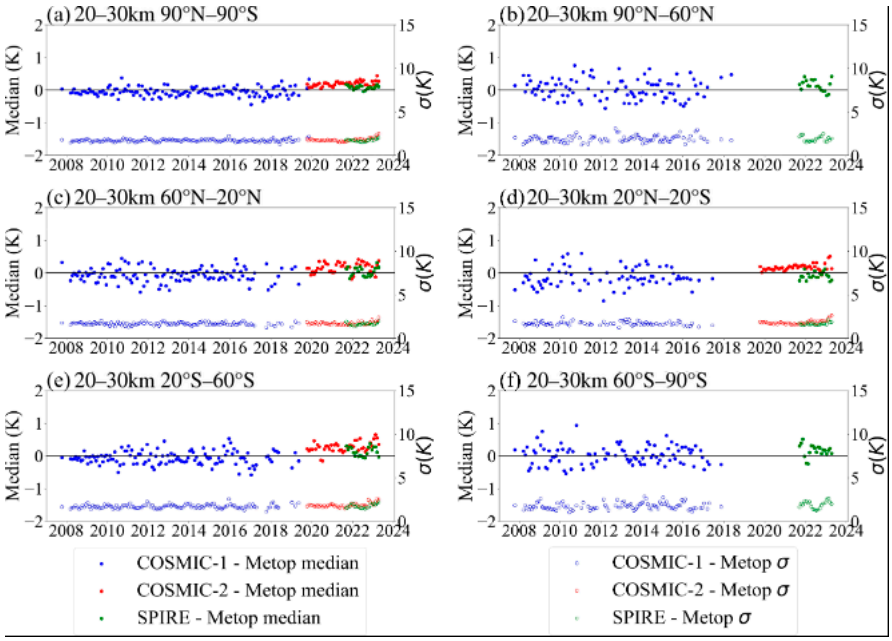


Figure 15. Measures of temperature consistency for collocated COSMIC-1–MetOp (blue), COSMIC-2–MetOp (red), and Spire–MetOp (green) pairs in the 20–30 km layer for (**a**) the globe (90°N–90°S), (**b**) Northern Hemisphere polar region (NHP, 90°N–60°N), (**c**) Northern Hemisphere subtropics and midlatitudes (NHSM, 60°N–20°N), (**d**) tropics (TRO, 20°N–20°S), (**e**) Southern Hemisphere subtropics and midlatitudes (SHSM, 20°S–60°S), and (**f**) Southern Hemisphere polar region (SHP, 60°S–90°S). COSMIC-2 data cover 45°N–20°N in NHSM and 20°S–45°S in SHSM.

Figure 15 shows the seasonal structure of differences between COSMIC-2 and MetOp GRAS temperatures in the 20–30 km layer, particularly in the COSMIC-2 midlatitude domains (45°N–20°N and 20°S–45°S). Figure 15 showed a good agreement between MetOp and COSMIC-1, and generally good agreement with Spire, particularly within the latitude range sampled by COSMIC-2. In contrast, COSMIC-2 exhibited more pronounced height-dependent differences above approximately 20 km and seasonal structure in the subtropical latitude bands. Some Spire–MetOp differences were also identified at high latitudes; therefore, we do not imply that MetOp agrees perfectly with every other mission or constitutes an error-free reference. However, COSMIC-2 shows larger differences from MetOp and also differs from other missions. Both the mean temperature difference and the standard deviation for COSMIC-2–MetOp pairs increase with altitude from 15 to 30 km (Figure 16).

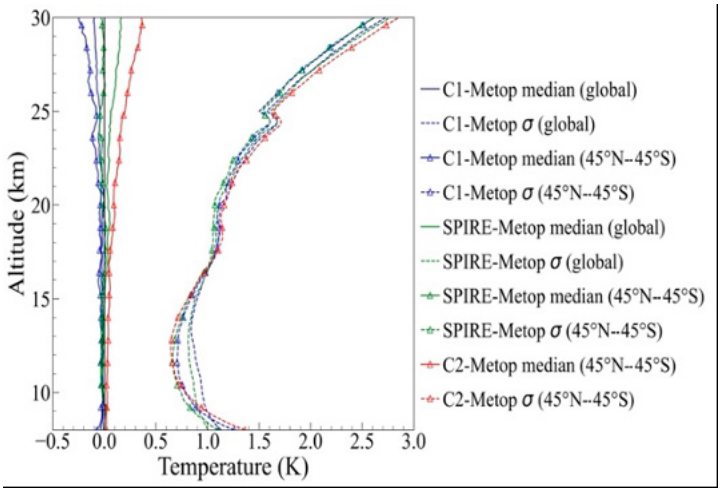


Figure 16. Measures of consistency between collocated COSMIC-1 and MetOp (blue), Spire and MetOp (green), and COSMIC-2 and MetOp pairs (red) as a function of height for the globe and the 45°N–45°S region. The central 68% range is defined as the interval centered on the median that contains 68% of the counts, whose half-width is approximately one standard deviation for a Gaussian distribution (Figure 7 of [22]).

Note that the tangent-point drift in oblique COSMIC-2 occultations may contribute to the height- and season-dependent differences through interactions with horizontal atmospheric gradients (see Foelsche et al. [69]). Foelsche et al. [69] stated that oblique RO profiles, owing to the viewing geometry (more side viewing), introduce representativeness differences, particularly where horizontal atmospheric gradients are strong (which may violate the symmetry atmosphere assumption for RO retrieval). The current bending angle forward model is in 1D. In a simulation study, Foelsche et al. [69] demonstrated that accounting for the 3-D tangent-point trajectory can substantially reduce such errors. This mechanism, together with residual ionospheric effects, sampling differences, and processing choices, remains under investigation.

Because the COSMIC-2–MetOp differences have seasonal and height-dependent structure (Figure 15), COSMIC-2 was excluded from the STAR-ROPP multi-mission environmental data record examined by Zhou et al. [22]. This decision illustrates that a mission may be valuable for NWP but require further consistency assessment before inclusion in a long-term climate record. Figure 17 compares vertical temperature trends from the STAR-ROPP record with those from ERA5, JRA-55, and MERRA-2; the records generally have similar vertical trend structures.

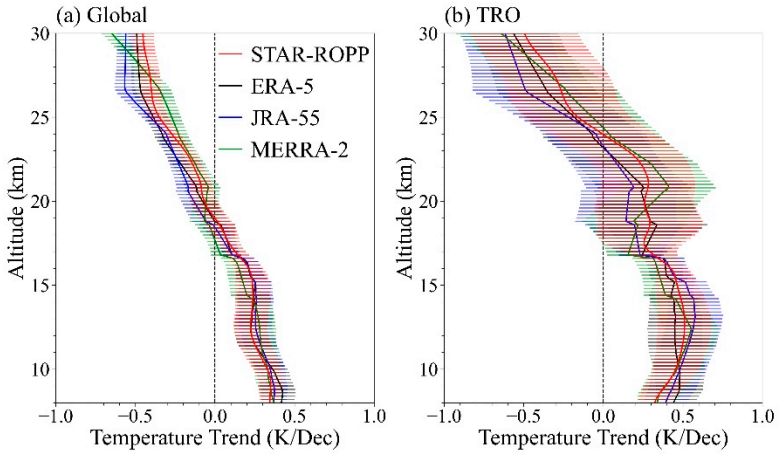


Figure 17. Vertically resolved temperature trends for September 2006–July 2023 estimated from STAR-ROPP (red), ERA5 (black), JRA-55 (blue), and MERRA-2 (green) for (**a**) the globe (90°S–90°N) and (**b**) the tropics (TRO, 20°S–20°N). Error bars represent trend uncertainty at the 95% confidence level (Figure 14 of [22]).

4.3. Tropospheric Water-Vapor Variability and Trends from COSMIC-1 RO

GNSS RO water-vapor products are retrieved by separating the dry-air and water-vapor contributions to refractivity using a priori atmospheric information. Shao et al. [70] evaluated UCAR COSMIC-1 WETPrf retrievals against collocated ERA5 water vapor at 300, 500, and 850 hPa from 2007 to 2018, where WETPrf retrievals used ERA-Interim as their first guess. Comparison results show that WETPrf is much closer to ERA5 than to ERA-Interim [70].

Shao et al. [70] also found that the WETPrf and ERA5 generally agreed on large-scale spatial and temporal variability, with COSMIC-1 water-vapor retrievals slightly lower than ERA5 at 500 and 850 hPa. These relative differences do not establish an absolute dry

bias in COSMIC-1 or exclude a wet bias in ERA5. They may reflect uncertainties in either dataset, retrieval-background dependence, and representativeness differences. Additional observational comparisons are needed to determine their respective contributions.

Using sampling-error-adjusted time series, Shao et al. [70] reported positive global COSMIC-1 water-vapor trends of 3.47 ± 1.77, 3.25 ± 1.25, and 2.03 ± 0.65% decade − 1 at 300, 500, and 850 hPa, respectively. Regional differences between COSMIC-1 and ERA5 were larger in some tropical and subtropical areas, especially at 850 hPa in convection- and stratocumulus-affected regions. These results indicate that RO-derived water-vapor records can complement reanalyses by resolving vertical and regional variability. However, climate interpretation requires a consistent retrieval configuration, explicit control of changing sampling, attention to lower-tropospheric super-refraction and background dependence, and independent comparison [70].

Note that many studies explicitly justified using ECMWF reanalysis for RO humidity comparisons because it combines many observing systems and assigns relatively large RO uncertainties in the middle and lower troposphere (Rieckh et al. [71]; Zhang et al. [72]; Poli et al. [73]). For example, Zhang et al. [72] explain that larger assigned observation errors reduce the influence of RO observations in the tropical lower troposphere for ECMWF reanalysis. They identify measurement uncertainty, atmospheric representativeness, and forward-operator errors as relevant contributors. Moisture gradients, horizontal inhomogeneity, and complex propagation conditions make these errors particularly challenging near the boundary layer. Their experiments show that assigning errors separately for individual profiles can improve assimilation performance. In this case, the larger assumed observation-error variances reduce the penalty for departures from RO observations. Consequently, the ERA5 can remain closer to the model background and other observational constraints.

4.4. Monitoring PBLH Variations Using Multi-Mission RO Data

Studies [74–76] indicate that high-resolution profiles from multiple RO missions provide consistent PBL-height estimates. Figure 18 compares gridded COSMIC-2 and Spire PBLH over three marine stratocumulus regions during June–August 2022. RO PBLH estimates have also been compared with radiosonde, lidar, CALIOP, and reanalysis estimates [76–80]. The COSMIC-2–Spire agreement provides evidence of cross-mission consistency for the examined period and regions; however, constructing a climate-quality record also requires long-term stability, sampling correction, and independent validation.

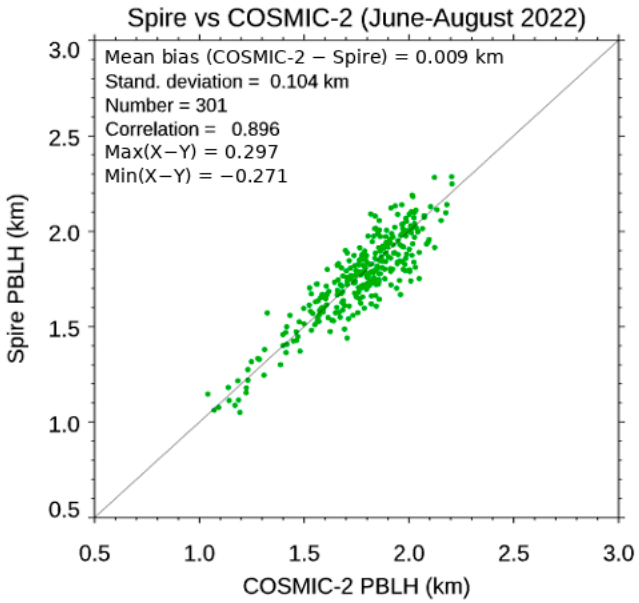


Figure 18. Scatterplot of Spire versus COSMIC-2 mean PBLH in the three marine stratocumulus cloud-dominated regions [SE Pacific (15–25°S, 70–85°W), SE Atlantic (5–25°S, 0–20°W), and SE Indian Ocean (15–35°S, 70–112°E)] combined during June–August 2022 after binning to 2° × 2° global grids.

In summary, the reviewed applications indicate that a common retrieval chain can reveal coherent temperature, moisture, and boundary-layer variability across missions. However, careful inter-mission stability assessment, sampling correction, and mission-specific uncertainty characterization are required before combining all RO missions into a climate data record.

5. Remaining Challenges and Research Outlook

5.1. Adaptive Processing Cutoffs and Retention of Lower-Atmospheric Information

The cutoff height for GNSS RO excess-phase processing determines how much lower-atmospheric signal is retained for bending-angle and refractivity retrievals. SNR generally decreases as the signal traverses denser atmospheric layers, but a low-SNR threshold alone cannot distinguish recoverable lower-atmospheric information from noise or multipath. The appropriate cutoff also depends on receiver sensitivity, mission altitude, viewing geometry, atmospheric conditions, sampling, and processing.

The research need is to develop an adaptive, mission-aware balance between retaining lower-atmospheric information and limiting retrieval noise and bias. Impact-parameter filtering can reduce inversion noise but may remove useful sub-signals with larger bending angles [81,82], whereas empirical approaches can relate cutoff selection to observed SNR and bending-angle noise [83]. Operational Sentinel-6A assessments further indicate that cutoff strategy and processor changes can materially alter tropospheric data retention [84]. Future evaluations should compare alternative cutoff strategies using common reference data, matched atmospheric regimes, and downstream NWP or PBL metrics rather than judge them only by the number of profiles that penetrate to a specified height.

STAR uses the Full Spectrum Inversion method to retrieve bending-angle and refractivity profiles [15]. Applying this capability across missions provides a controlled basis for separating receiver and sampling differences from processing effects. Inter-center comparisons indicate that retrieval-algorithm choices can affect lower-tropospheric refractivity and penetration [85]. Matched tests are therefore needed to determine whether

a cutoff strategy preserves useful lower-tropospheric information without increasing bias or uncertainty.

5.2. Water-Vapor Retrievals Under Super-Refraction and Ducting

Despite successful RO-based PBL-height detection in many regions, accurate retrieval of lower-tropospheric thermal and moisture structure remains challenging because super-refraction and ducting can produce negative refractivity biases, especially over the subtropical eastern oceans [83,86–89]. Proposed correction strategies use collocated precipitable-water information from microwave radiometers [90] or grazing signals from the same RO event [91]. Collocated ground-based GNSS and microwave radiometer (MWR) measurements also offer a complementary approach to evaluating lower-tropospheric RO moisture corrections. Parde et al. [92] demonstrated improved GNSS precipitable-water retrieval in the Eastern Mediterranean by using MWR-derived thermodynamic information to estimate the weighted-mean atmospheric temperature. Ground-based GNSS can constrain column-integrated moisture, whereas profiles provide complementary vertical information. Such measurements could support cross-mission validation, provided that correction-development and validation samples are separated and that differences in sampling, vertical sensitivity, and atmospheric-column coverage are addressed. Column agreement alone does not establish accurate moisture structure below 2 km. Further evaluation is needed to assess not only individual corrections but also their robustness across missions, viewing geometries, atmospheric regimes, and processing systems, using independent validation and explicit uncertainty estimates.

5.3. Uncertainty-Aware Quality Control and Observation-Error Models

Large background departures may reflect observation error, forward-operator limitations, atmospheric representativeness, or model error. In super-refractive layers, where the vertical refractivity gradient exceeds the critical magnitude, conventional Abel inversion becomes nonunique [93]. Current systems use background refractivity gradients and other quality-control procedures to identify affected observations, but this treatment can reject potentially useful information below and near the PBL. A priority is to move from largely altitude- and platform-based error specifications toward uncertainty-aware weighting that also reflects atmospheric structure, viewing geometry, retrieval diagnostics such as Local spectral width (LSW) or Dynamic bending-angle observation error (DBAOE), vertical error correlation, and forward-operator limitations. Such models must be calibrated and tested within data-assimilation systems rather than inferred solely from departures from one reference.

5.4. Multi-Mission Climate Continuity, Reprocessing, and Stewardship

Long-term records face a different risk: changes in mission mix, sampling, receiver characteristics, or processing can appear as geophysical change. The review therefore supports sustained reprocessing with a common algorithmic framework, routine overlap comparisons, and mission-specific stability monitoring. Inter-mission differences should be evaluated as functions of height, latitude, season, local time, and relevant viewing geometry before a mission transition is included in a climate record.

A climate-ready archive also requires reproducible processing, retained quality-control and uncertainty metadata, transparent versioning, and periodic comparison with independent observations and reanalyses. Uncertainty can be propagated from individual profiles through sampling and aggregation to gridded atmospheric fields [23]. These practices link operational stewardship with scientific traceability and allow future reprocessing when improved retrieval algorithms become available.

5.5. NOAA Readiness for an Operational Expanding Multi-Mission Observing System

Like other satellite observations, NESDIS supports GNSS RO through operational processing, science development, user support, archiving, and stewardship. The STAR GNSS RO program (https://gpsmet.umd.edu/gnssro/index.php (accessed on 5 November 2024)) serves as a science and data center for NESDIS in-house processing, enterprise algorithm development, and applications. Its independent inversion packages and routinely processed products provide both an operational capability and a reference pathway for cross-mission evaluation (Table 4; https://gpsmet.umd.edu/gnssro/download.php (accessed on 5 November 2024)).

NOAA has committed to the continued purchase of commercial GNSS RO data. In September 2025, NOAA NESDIS Commercial Data Program (CDP) announced the purchase of 10,000 GNSS RO profiles and 2500 TEC ionospheric measurements per day, with unlimited data rights, to support weather forecasting and space-weather applications. Over the next 5–10 years, additional GNSS RO and GNSS reflectometry sensors, together with more signals from GPS III, Galileo, Beidou, GLONASS, IRNSS, QZSS, and other systems, will expand the volume and heterogeneity of available observations. Operational readiness will therefore depend on scalable processing, automated quality monitoring, traceable metadata, and rapid mission-to-mission intercomparison.

Table 4. Average daily numbers of RO profiles processed by the STAR GNSS RO program for the listed missions.

Mission	RO per Day
COSMIC-2	5000
PlanetiQ	7000
Spire	3000
KOMPSAT-5	500
PAZ	200
GRAS MetOp-A	300
GRAS MetOp-B	500
GRAS MetOp-C	500
COSMIC-1	2500
TanDEM-X	500

Current missions have led to follow-on systems, including EUMETSAT MetOp Second Generation, Sentinel-6B, PlanetiQ GNOMES, new Spire missions, and the YunYao, Fengyun-3, and Tianmu series. These systems increase the number of receivers, tracked GNSS signals, sampling patterns, and processing requirements. NOAA also plans future satellite systems [94]. The central design question is how to balance per-profile measurement quality, observation volume, geographic and local-time coverage, latency, processing consistency, and long-term continuity across this mixed architecture.

5.6. Outlooks on Priorities for the Next Phase

The preceding review identifies five linked priorities. Table 5 frames them as testable questions and evaluation criteria so that future mission, processing, and application studies can be compared on a common basis. Each priority targets an intervening link in the pathway and is evaluated by its effect on retrieval quality, usable yield, or application value.

Table 5. Outlook for the future priorities for multi-mission GNSS RO research and operations.

Priority	Research or Operational Question	Evaluation Criterion
Lower-atmospheric signal retention	How should cutoff, filtering, and wave-optics processing adapt to mission design and atmospheric regime?	Greater usable penetration without increased retrieval bias or uncertainty
Dynamic uncertainty and quality control	Can retrieval diagnostics and environmental indicators support profile- or regime-dependent error weighting?	Calibrated departures and increased beneficial lower-tropospheric use in data assimilation
Super-refraction and ducting	When can auxiliary precipitable-water or grazing-signal information correct refractivity and moisture biases?	Robust improvement across missions and independent reference datasets
Climate continuity	How can mission transitions, sampling changes, and processing updates be prevented from contaminating long-term records?	Demonstrated stability, overlap consistency, sampling control, and reproducible reprocessing
Observing-system design	What balance of measurement quality, profile volume, coverage, latency, and continuity maximizes application value?	Consistent incremental impact across FSOI, OSE, regional, and environmental-product evaluations

6. Conclusions

This review supports evaluating multi-mission GNSS RO as an observing system rather than as a set of missions ranked by a single instrument metric. The evidence supports an evaluation pathway in which antenna design, orbit, viewing geometry, signal sampling, and SNR relate to tracking and penetration; atmospheric structure and processing contribute to retrieval bias and uncertainty; and complementarity influences application value. The reviewed comparisons show that higher SNR generally improves tracking and lower-tropospheric penetration but does not by itself remove biases and uncertainty arising from water-vapor irregularity, multipath, super-refraction, departures from spherical symmetry, or processing choices.

Current results indicate that commercial Spire and PlanetiQ observations are broadly compatible with COSMIC-2 and partner missions in the atmospheric layers and that their additional sampling can benefit global and regional NWP. Section 4.2 showed that the selected, consistently processed multi-mission RO observations support climate-record construction after accounting for mission-dependent biases, sampling differences, and temporal stability. Because the COSMIC-2–MetOp differences have seasonal and height-dependent structure, and MetOp is consistent with COSMIC-1 and other missions, we excluded COSMIC-2 from the STAR-ROPP multi-mission environmental data record. This indicates that we need to assess consistency before including RO missions in a long-term climate record.

The next phase should prioritize adaptive lower-atmospheric processing, improved treatment of super-refraction, uncertainty-aware quality control and observation-error

models, sustained common reprocessing and intercomparison, and observing-system design that jointly considers quality, volume, coverage, latency, and continuity. Here, common reprocessing means consistent processing across missions and time within a defined product, complemented by comparisons among independent processing centers to quantify structural uncertainty. This evaluation pathway framework offers a practical basis for NOAA/STAR and the wider GNSS RO community to evaluate new commercial and partner missions without conflating signal strength, retrieval performance, and scientific or operational value.

International collaboration is essential to sustaining a consistent multi-mission RO record. Existing examples include the NOAA–Taiwan COSMIC-2 partnership and coordinated processing and evaluation through Radio Occultation Modeling Experiment (ROMEX). The EUMETSAT ROM SAF (Radio Occultation Meteorology Satellite Application Facility) also contributes community processing software and reprocessed climate products. Future cooperation should facilitate access to historical low-level observations, documented processing configurations, shared benchmark datasets, and coordinated assessments of mission transitions.

Author Contributions: All authors contributed to the preparation, review, and editing of the manuscript. All authors have read and agreed to the published version of the manuscript.

Funding: The contributions of authors affiliated with the Cooperative Institute for Satellite Earth System Studies at the University of Maryland/ESSIC were supported by the National Oceanic and Atmospheric Administration under grants NA19NES4320002 and NA24NESX432C0001.

Data Availability Statement: The STAR GNSS RO program processed dry-temperature profiles from multiple GNSS RO missions; these products are publicly available at https://gpsmet.umd.edu/gnssro/download.php (accessed on 5 November 2024). The ROM SAF environmental data record is available at https://rom-saf.eumetsat.int/product_archive.php (accessed on 5 November 2024). ERA5 data are available at https://cds.climate.copernicus.eu/datasets/reanalysis-era5-pressure-levels (accessed on 5 November 2026). UCAR data are available at https://cdaac-www.cosmic.ucar.edu/cdaac/products.html (accessed on 5 November 2024). The HWRF simulation datasets and software used in the cited STAR studies are stored on NOAA research and development high-performance computing systems and University of Maryland Linux servers and are available upon request.

Acknowledgments: Disclaimer: The scientific results and conclusions, as well as any views or opinions expressed herein, are those of the authors and do not necessarily reflect those of NOAA or the Department of Commerce. Generative SI Disclosure: Generative SI tools were used to improve clarity, correct grammatical errors, and format the references.

Conflicts of Interest: Authors Jun Zhou and Xinjia Zhou are employed by Entarian LLC. The authors declare no other competing interests.

Abbreviations

Abbreviation	Meaning
3CH	Three-cornered-hat method
ATBD	Algorithm Theoretical Basis Document
BA	Bending angle
CALIOP	Cloud–Aerosol Lidar with Orthogonal Polarization
CDAAC	COSMIC Data Analysis and Archive Center
CDP	Commercial Data Program
CHAMP	Challenging Minisatellite Payload
CISESS	Cooperative Institute for Satellite Earth System Studies

COSMIC	Constellation Observing System for Meteorology, Ionosphere, and Climate
COSMIC-1/COSMIC-2	First and second COSMIC missions, respectively
CWDP	Commercial Weather Data Program
DA	Data assimilation
DBAOE	Dynamic bending-angle observation error
DO	Delivery order
ECMWF	European Centre for Medium-Range Weather Forecasts
EPH	Experiment assimilating conventional observations plus GNSS RO refractivity; an experiment label
ERA5	Fifth-generation ECMWF atmospheric reanalysis
EUMETSAT	European Organisation for the Exploitation of Meteorological Satellites
FORMOSAT	Formosa Satellite; Taiwanese satellite mission series
FSI	Full Spectrum Inversion
FSOI	Forecast Sensitivity to Observation Impact
GFS	Global Forecast System
GLONASS	Globalnaya Navigatsionnaya Sputnikovaya Sistema; Russian global navigation satellite system
GNSS	Global Navigation Satellite System
GPS	Global Positioning System
GRACE	Gravity Recovery and Climate Experiment
GRAS	GNSS Receiver for Atmospheric Sounding
GTS	Global Telecommunication System; also the label for the conventional-observation experiment
HAFS	Hurricane Analysis and Forecasting System
HWRF	Hurricane Weather Research and Forecasting model
IRNSS	Indian Regional Navigation Satellite System
IRT	Infrared radiances sensitive to temperature; Figure 10 category
IRWV	Infrared radiances sensitive to water vapor; Figure 10 category
JRA-55	Japanese 55-year Reanalysis
KOMPSAT-5	Korea Multi-Purpose Satellite-5
L1/L2	GNSS carrier-frequency bands or signals
LSW	Local spectral width
MERRA-2	Modern-Era Retrospective Analysis for Research and Applications, Version 2
MetOp	Meteorological Operational satellite series
MLS	Microwave Limb Sounder
MWR	Microwave Radiometer
MWT	Microwave radiances sensitive to temperature
MWWV	Microwave radiances sensitive to water vapor, cloud, and precipitation
NASA	National Aeronautics and Space Administration
NavIC	Navigation with Indian Constellation
NCEP	National Centers for Environmental Prediction
NESDIS	National Environmental Satellite, Data, and Information Service
NHP	Northern Hemisphere polar region
NHSM	Northern Hemisphere subtropics and midlatitudes
NOAA	National Oceanic and Atmospheric Administration
NWP	Numerical weather prediction
OSE/OSEs	Observing-system experiment/experiments
PBL	Planetary boundary layer
PBLH	Planetary-boundary-layer height
PMIN	Minimum central sea-level pressure
POD	Precise orbit determination
QC/QCs	Quality control/quality controls
QZSS	Quasi-Zenith Satellite System

RMSD	Root-mean-square deviation
RO	Radio occultation
RODB	Radio Occultation Data Buy
ROM SAF	Radio Occultation Meteorology Satellite Application Facility
ROMEX	Radio Occultation Modeling Experiment
ROPP	Radio Occultation Processing Package
SDC	Science Data Center; the STAR GNSS RO center identified in the manuscript
SE	Southeastern; geographical qualifier in Figure 18
SEM	Standard error of the mean
SHP	Southern Hemisphere polar region
SHSM	Southern Hemisphere subtropics and midlatitudes
SNR	Signal-to-noise ratio
STAR	Center for Satellite Applications and Research
STAR-ROPP	STAR-configured Radio Occultation Processing Package
TanDEM-X	TerraSAR-X add-on for Digital Elevation Measurement
TC/TCs	Tropical cyclone/cyclones
TEC	Total electron content
TGRS	Tri-GNSS Radio-occultation System
TRO	Tropical region
UCAR	University Corporation for Atmospheric Research
UKMET	UK Met Office; shorthand used for its forecast system
UTLS	Upper troposphere and lower stratosphere
V/V	Voltage-to-voltage ratio
WETPrf	UCAR/CDAAC wet-atmosphere profile product
WRF	Weather Research and Forecasting model

References

1. Anthes, R.A.; Bernhardt, P.A.; Chen, Y.; Cucurull, L.; Dymond, K.F.; Ector, D.; Healy, S.B.; Ho, S.-P.; Hunt, D.C.; Kuo, Y.-H.; et al. The COSMIC/FORMOSAT-3 Mission: Early Results. *Bull. Am. Meteorol. Soc.* **2008**, *89*, 313–333. https://doi.org/10.1175/BAMS-89-3-313.
2. Anthes, R.A. Exploring Earth's Atmosphere with Radio Occultation: Contributions to Weather, Climate, and Space Weather. *Atmos. Meas. Tech.* **2011**, *4*, 1077–1103. https://doi.org/10.5194/amt-4-1077-2011.
3. Ho, S.-P.; Anthes, R.A.; Ao, C.O.; Healy, S.; Horányi, A.; Hunt, D.; Mannucci, A.J.; Pedatella, N.; Randel, W.J.; Simmons, A.; et al. The COSMIC/FORMOSAT-3 Radio Occultation Mission after 12 Years: Accomplishments, Remaining Challenges, and Potential Impacts of COSMIC-2. *Bull. Am. Meteorol. Soc.* **2020**, *101*, E1107–E1136. https://doi.org/10.1175/BAMS-D-18-0290.1.
4. Steiner, A.K.; Ladstädter, F.; Ao, C.O.; Gleisner, H.; Ho, S.-P.; Hunt, D.; Schmidt, T.; Foelsche, U.; Kirchengast, G.; Kuo, Y.-H.; et al. Consistency and Structural Uncertainty of Multi-Mission GPS Radio Occultation Records. *Atmos. Meas. Tech.* **2020**, *13*, 2547–2575. https://doi.org/10.5194/amt-13-2547-2020.
5. Scherllin-Pirscher-, B.; Steiner, A.K.; Anthes, R.A.; Alexander, M.J.; Alexander, S.P.; Biondi, R.; Birner, T.; Kim, J.; Randel, W.J.; Son, S.-W.; et al. Tropical Temperature Variability in the UTLS: New Insights from GPS Radio Occultation Observations. *J. Clim.* **2021**, *34*, 2813–2838. https://doi.org/10.1175/JCLI-D-20-0385.1.
6. Ho, S.-P.; Zhou, X.; Shao, X.; Zhang, B.; Adhikari, L.; Kireev, S.; He, Y.; Yoe, J.G.; Xia-Serafino, W.; Lynch, E. Initial Assessment of the COSMIC-2/FORMOSAT-7 Neutral Atmosphere Data Quality in NESDIS/STAR using in situ and satellite data. *Remote Sens.* **2020**, *12*, 4099. https://doi.org/10.3390/rs12244099.
7. Ho, S.-P.; Pedatella, N.; Foelsche, U.; Healy, S.; Weiss, J.-P.; Ullman, R. Using Radio Occultation Data for Atmospheric Numerical Weather Prediction, Climate Sciences, and Ionospheric Studies and Initial Results from COSMIC-2, Commercial RO Data, and Recent RO Missions. *Bull. Am. Meteorol. Soc.* **2022**, *103*, E2506–E2512. https://doi.org/10.1175/BAMS-D-22-0174.1.
8. Ho, S.-P.; Zhou, X.; Shao, X.; Chen, Y.; Jing, X.; Miller, W. Using the Commercial GNSS RO Spire Data in the Neutral Atmosphere for Climate and Weather Prediction Studies. *Remote Sens.* **2023**, *15*, 4836. https://doi.org/10.3390/rs15194836.
9. Ho, S.-P.; Kireev, S.; Shao, X.; Zhou, X.; Jing, X. Processing and Validation of the STAR COSMIC-2 Temperature and Water Vapor Profiles in the Neutral Atmosphere. *Remote Sens.* **2022**, *14*, 5588. https://doi.org/10.3390/rs14215588.

10. Chang, H.; Lee, J.; Yoon, H.; Morton, Y.J.; Saltman, A. Performance Assessment of Radio Occultation Data from GeoOptics by Comparing with COSMIC Data. *Earth Planets Space* **2022**, *74*, 108. https://doi.org/10.1186/s40623-022-01667-6.
11. Qiu, C.; Wang, X.; Zhou, K.; Zhang, J.; Chen, Y.; Li, H.; Liu, D.; Yuan, H. Comparative Assessment of Spire and COSMIC-2 Radio Occultation Data Quality. *Remote Sens.* **2023**, *15*, 5082. https://doi.org/10.3390/rs15215082.
12. Zhran, M.; Mousa, A.; Wang, Y.; Hasher, F.F.B.; Jin, S. Assessment of Commercial GNSS Radio Occultation Performance from PlanetiQ Mission. *Remote Sens.* **2024**, *16*, 3339. https://doi.org/10.3390/rs16173339.
13. Ganeshan, M.; Wu, D.L.; Santanello, J.A.; Gong, J.; Ao, C.; Vergados, P.; Nelson, K.J. Exploring Commercial Global Navigation Satellite System (GNSS) Radio Occultation (RO) Products for Planetary Boundary Layer Studies in the Arctic. *Atmos. Meas. Tech.* **2025**, *18*, 1389–1403. https://doi.org/10.5194/amt-18-1389-2025.
14. Anthes, R.A.; Sjoberg, J.; Starr, J.; Zeng, Z. Evaluation of Biases and Uncertainties in ROMEX Radio Occultation Observations. *Atmos. Meas. Tech.* **2025**, *18*, 6997–7019. https://doi.org/10.5194/amt-18-6997-2025.
15. Chen, Y.; Zhou, X.; Jing, X.; Ho, S.-P.; Shao, X.; Liu, T.-C. Processing Multiple GNSS RO Data Using FSI and ROPP: Results from the ROMEX. *Atmos. Meas. Tech.* **2026**, *19*, 3781–3800. https://doi.org/10.5194/amt-19-3781-2026.
16. Bowler, N.E. An Assessment of GNSS Radio Occultation Data Produced by Spire. *Q. J. R. Meteorol. Soc.* **2020**, *146*, 3772–3788. https://doi.org/10.1002/qj.3872.
17. Miller, W.J.; Chen, Y.; Ho, S.-P.; Shao, X. Exploring the Value of Spire GNSS Radio Occultation Bending Angle Assimilation for Improving HWRF Model Forecasts of Atlantic Hurricane Intensity. *Weather Forecast.* **2025**, *40*, 809–827. https://doi.org/10.1175/WAF-D-24-0092.1.
18. Zhang, H.; Shao, H.; Ruston, B.; Braun, J.J. Impact Study of Increased Radio Occultation Observations during the ROMEX Period Using JEDI and the GFS Atmospheric Model. *Atmos. Meas. Tech.* **2025**, *18*, 6167–6184. https://doi.org/10.5194/amt-18-6167-2025.
19. Bowler, N.E.; Lewis, O. Experiments with a Large Number of GNSS-RO Observations through the ROMEX Collaboration in the Met Office NWP System. *Atmos. Meas. Tech.* **2026**, *19*, 2479–2505. https://doi.org/10.5194/amt-19-2479-2026.
20. Miller, W.J.; Chen, Y.; Ho, S.-P.; Shao, X. How Does Assimilating a Large Commercial GNSS RO Dataset Impact HAFS Hurricane Forecasts? An Evaluation in Support of the ROMEX Experiment. *Atmos. Meas. Tech.* **2026**, *19*, 4833–4851. https://doi.org/10.5194/amt-19-4833-2026.
21. Jing, X.; Ho, S.-P.; Shao, X.; Liu, T.-C.; Chen, Y.; Zhou, X. Spire RO Thermal Profiles for Climate Studies: Initial Comparisons of the Measurements from Spire, NOAA-20 ATMS, Radiosonde, and COSMIC-2. *Remote Sens.* **2023**, *15*, 3710. https://doi.org/10.3390/rs15153710.
22. Zhou, J.; Ho, S.-P.; Zhou, X.; Shao, X.; Gu, G.; Chen, Y.; Liu, T.-C.; Jing, X. Construction of Temperature Climate Data Records in the Upper Troposphere and Lower Stratosphere Using Multiple RO Missions From September 2006 to July 2023 at NESDIS/STAR. *J. Geophys. Res. Atmos.* **2025**, *130*, e2024JD041295. https://doi.org/10.1029/2024JD041295.
23. Scher, S.; Ladstädter, F.; Schwärz, M.; Innerkofler, J.; Kirchengast, G. Uncertainty Propagation from Radio Occultation Profiles to Aggregated Atmospheric Gridded Fields. *Earth Space Sci.* **2026**, *13*, e2025EA004389. https://doi.org/10.1029/2025EA004389.
24. Chen, Y.; Shao, X.; Cao, C.; Ho, S.-P. Simultaneous Radio Occultation Predictions for Inter-Satellite Comparison of Bending Angle Profiles from COSMIC-2 and GeoOptics. *Remote Sens.* **2021**, *13*, 3644. https://doi.org/10.3390/rs13183644.
25. Miller, W.J.; Chen, Y.; Ho, S.-P.; Shao, X. Evaluating the Impacts of COSMIC-2 GNSS RO Bending Angle Assimilation on Atlantic Hurricane Forecasts Using the HWRF Model. *Mon. Weather Rev.* **2023**, *151*, 1821–1847. https://doi.org/10.1175/MWR-D-22-0198.1.
26. Bai, W.; Wang, G.; Huang, F.; Sun, Y.; Du, Q.; Xia, J.; Wang, X.; Meng, X.; Hu, P.; Yin, C.; et al. Review of Assimilating Spaceborne Global Navigation Satellite System Remote Sensing Data for Tropical Cyclone Forecasting. *Remote Sens.* **2025**, *17*, 118. https://doi.org/10.3390/rs17010118.
27. Gorbunov, M.; Irisov, V.; Rocken, C. Noise Floor and Signal-to-Noise Ratio of Radio Occultation Observations: A Cross-Mission Statistical Comparison. *Remote Sens.* **2022**, *14*, 691. https://doi.org/10.3390/rs14030691.
28. Turbiner, D.; Young, L.E.; Meehan, T.K. Phased Array GNSS Antenna for the FORMOSAT-7/COSMIC-2 Radio Occultation Mission. In Proceedings of the 25th International Technical Meeting of the Satellite Division of the Institute of Navigation (ION GNSS 2012), Nashville, TN, USA, 17–21 September 2012; pp. 915–916.
29. Schreiner, W.S.; Weiss, J.-P.; Anthes, R.A.; Braun, J.; Chu, V.; Fong, J.; Hunt, D.; Kuo, Y.-H.; Meehan, T.; Serafino, W.; et al. COSMIC-2 Radio Occultation Constellation: First Results. *Geophys. Res. Lett.* **2020**, *47*, e2019GL086841. https://doi.org/10.1029/2019GL086841.

30. Anthes, R.A.; Marquardt, C.; Ruston, B.; Shao, H. Radio Occultation Modeling Experiment (ROMEX): Determining the impact of radio occultation observations on numerical weather prediction. *Bull. Am. Meteorol. Soc.* **2024**, *105*, E1552–E1568. https://doi.org/10.1175/BAMS-D-23-0326.1.
31. Mo, Z.; Lou, Y.; Zhang, W.; Zhou, Y.; Wu, P.; Zhang, Z. Performance assessment of multi-source GNSS radio occultation from COSMIC-2, MetOp-B/C, FY-3D/E, Spire, and PlanetiQ over China. *Atmos. Res.* **2024**, *311*, 107704. https://doi.org/10.1016/j.atmosres.2024.107704.
32. Ao, C.O.; Wang, K.-N.; Hajj, G.A. PBL Remote Sensing with GNSS-RO. In Proceedings of IROWG-10, Boulder, CO, USA, 12–18 September 2024. Available online: https://www.cosmic.ucar.edu/sites/default/files/2024-09/19%20-%20Ao_Chi_2024.09.16.pptx.pdf (accessed on 5 November 2025).
33. Lonitz, K.; Marquardt, C.; Bowler, N.; Healy, S. *Final Technical Note of 'Impact Assessment of Commercial GNSS-RO Data'*; ESA Contract Report No. 4000131086/20/NL/FF/a; European Centre for Medium-Range- Weather Forecasts (ECMWF): Reading, UK, 2021. https://doi.org/10.21957/wrh6voyyi (accessed on 1 January 2022).
34. Langland, R.H.; Baker, N.L. Estimation of observation impact using the NRL atmospheric variational data assimilation adjoint system. *Tellus A* **2004**, *56*, 189–201. https://doi.org/10.1111/j.1600-0870.2004.00056.x.
35. Cardinali, C. Monitoring the observation impact on the short-range forecast. *Q. J. R. Meteorol. Soc.* **2009**, *135*, 239–250. https://doi.org/10.1002/qj.366.
36. Cardinali, C.; Healy, S. Impact of GPS radio occultation measurements in the ECMWF system using adjoint-based diagnostics. *Q. J. R. Meteorol. Soc.* **2014**, *140*, 2315–2320. https://doi.org/10.1002/qj.2300.
37. Cucurull, L. Recent Impact of COSMIC-2 with Improved Radio Occultation Data Assimilation Algorithms. *Weather Forecast.* **2023**, *38*, 1829–1847. https://doi.org/10.1175/WAF-D-22-0186.1.
38. Ruston, B.; Healy, S. Forecast Impact of FORMOSAT-7/COSMIC-2 GNSS Radio Occultation Measurements. *Atmos. Sci. Lett.* **2021**, *22*, e1019. https://doi.org/10.1002/asl.1019.
39. Harnisch, F.; Healy, S.B.; Bauer, P.; English, S.J. Scaling of GNSS radio occultation impact with observation number using an ensemble of data assimilations. *Mon. Weather Rev.* **2013**, *141*, 4395–4413. https://doi.org/10.1175/MWR-D-13-00098.1.
40. Kuo, Y.-H.; Wee, T.-K.; Sokolovskiy, S.; Rocken, C.; Schreiner, W.; Hunt, D.; Anthes, R.A. Inversion and Error Estimation of GPS Radio Occultation Data. *J. Meteorol. Soc. Jpn.* **2004**, *82*, 507–531. https://doi.org/10.2151/jmsj.2004.507.
41. Nolan, D.S. What Is the Trigger for Tropical Cyclogenesis? *Aust. Meteorol. Mag.* **2007**, *56*, 241–266. https://doi.org/10.1071/ES06025.
42. Sippel, J.A.; Zhang, F. A Probabilistic Analysis of the Dynamics and Predictability of Tropical Cyclogenesis. *J. Atmos. Sci.* **2008**, *65*, 3440–3459. https://doi.org/10.1175/2008JAS2597.1.
43. Doyle, J.D.; Reynolds, C.A.; Amerault, C.; Moskaitis, J. Adjoint Sensitivity and Predictability of Tropical Cyclogenesis. *J. Atmos. Sci.* **2012**, *69*, 3535–3557. https://doi.org/10.1175/JAS-D-12-0110.1.
44. Teng, H.-F.; Kuo, Y.-H.; Done, J.M. Importance of Midlevel Moisture for Tropical Cyclone Formation in Easterly and Monsoon Environments over the Western North Pacific. *Mon. Weather Rev.* **2021**, *149*, 2449–2469. https://doi.org/10.1175/MWR-D-20-0313.1.
45. Zeng, Z.; Sokolovskiy, S.; Schreiner, W.S.; Hunt, D. Representation of Vertical Atmospheric Structures by Radio Occultation Observations in the Upper Troposphere and Lower Stratosphere: Comparison to High-Resolution Radiosonde Profiles. *J. Atmos. Ocean. Technol.* **2019**, *36*, 655–670. https://doi.org/10.1175/JTECH-D-18-0105.1.
46. Teng, H.-F.; Kuo, Y.-H.; Done, J.M. Potential Impacts of Radio Occultation Data Assimilation on Forecast Skill of Tropical Cyclone Formation in the Western North Pacific. *Geophys. Res. Lett.* **2023**, *50*, e2021GL096750. https://doi.org/10.1029/2021GL096750.
47. Chen, S.-Y.; Kuo, Y.-H.; Huang, C.-Y. The Impact of GPS RO Data on the Prediction of Tropical Cyclogenesis Using a Nonlocal Observation Operator: An Initial Assessment. *Mon. Weather Rev.* **2020**, *148*, 2701–2717. https://doi.org/10.1175/MWR-D-19-0286.1.
48. Liu, H.; Anderson, J.; Kuo, Y.-H. Improved Analyses and Forecasts of Hurricane Ernesto's Genesis Using Radio Occultation Data in an Ensemble Filter Assimilation System. *Mon. Weather Rev.* **2012**, *140*, 151–166. https://doi.org/10.1175/MWR-D-11-00024.1.
49. Charney, J.G.; Eliassen, A. On the Growth of the Hurricane Depression. *J. Atmos. Sci.* **1964**, *21*, 68–75. https://doi.org/10.1175/1520-0469(1964)021<0068:OTGOTH>2.0.CO;2.
50. Emanuel, K.A. An Air-Sea Interaction Theory for Tropical Cyclones. Part I: Steady-State Maintenance. *J. Atmos. Sci.* **1986**, *43*, 585–605. https://doi.org/10.1175/1520-0469(1986)043<0585:AASITF>2.0.CO;2.

51. Sjoberg, J.; Anthes, R.; Zhang, H. Estimating individual radio occultation uncertainties using the observations and environmental parameters. *J. Atmos. Ocean. Technol.* **2023**, *40*, 1461–1474. https://doi.org/10.1175/JTECH-D-23-0029.1.
52. Liu, H.; Kuo, Y.-H.; Sokolovskiy, S.; Zou, X.; Zeng, Z.; Hsiao, L.-F.; Ruston, B.C. A Quality Control Procedure Based on Bending Angle Measurement Uncertainty for Radio Occultation Data Assimilation in the Tropical Lower Troposphere. *J. Atmos. Ocean. Technol.* **2018**, *35*, 2117–2131. https://doi.org/10.1175/JTECH-D-17-0224.1.
53. Anthes, R.A.; Rieckh, T. Estimating Observation and Model Error Variances Using Multiple Data Sets. *Atmos. Meas. Tech.* **2018**, *11*, 4239–4260. https://doi.org/10.5194/amt-11-4239-2018.
54. Anthes, R.A.; Sjoberg, J.; Feng, X.; Syndergaard, S. Comparison of COSMIC and COSMIC-2 Radio Occultation Refractivity and Bending Angle Uncertainties in August 2006 and 2021. *Atmosphere* **2022**, *13*, 790. https://doi.org/10.3390/atmos13050790.
55. Sjoberg, J.P.; Anthes, R.A.; Rieckh, T. The Three-Cornered Hat Method for Estimating Error Variances of Three or More Atmospheric Datasets. Part I: Overview and Evaluation. *J. Atmos. Ocean. Technol.* **2021**, *38*, 555–572. https://doi.org/10.1175/JTECH-D-19-0217.1.
56. Bonafoni, S.; Biondi, R.; Brenot, H.; Anthes, R. Radio occultation and ground-based GNSS products for observing, understanding, and predicting extreme events: A review. *Atmos. Res.* **2019**, *230*, 104624. https://doi.org/10.1016/j.atmosres.2019.104624.
57. Babu, S.R.; Liou, Y.-A. Day-to-day variability of upper troposphere and lower stratosphere temperature in response to Taal volcanic eruption inferred from COSMIC-2 RO measurements. *J. Volcanol. Geotherm. Res.* **2022**, *421*, 107445. https://doi.org/10.1016/j.jvolgeores.2021.107445.
58. Randel, W.J.; Johnston, B.R.; Braun, J.J.; Sokolovskiy, S.; Vömel, H.; Podglajen, A.; Legras, B. Stratospheric Water Vapor from the Hunga Tonga–Hunga Ha'apai Volcanic Eruption Deduced from COSMIC-2 Radio Occultation. *Remote Sens.* **2023**, *15*, 2167. https://doi.org/10.3390/rs15082167.
59. Ho, S.-P.; Kirchengast, G.; Leroy, S.; Wickert, J.; Mannucci, A.J.; Steiner, A.K.; Hunt, D.; Schreiner, W.; Sokolovskiy, S.; Ao, C.O.; et al. Estimating the uncertainty of using GPS radio occultation data for climate monitoring: Intercomparison of CHAMP refractivity climate records from 2002 to 2006 from different data centers. *J. Geophys. Res. Atmos.* **2009**, *114*, D23107. https://doi.org/10.1029/2009JD011969.
60. Scherllin-Pirscher, B.; Kirchengast, G.; Steiner, A.K.; Kuo, Y.-H.; Foelsche, U. Quantifying Uncertainty in Climatological Fields from GPS Radio Occultation: An Empirical-Analytical Error Model. *Atmos. Meas. Tech.* **2011**, *4*, 2019–2034. https://doi.org/10.5194/amt-4-2019-2011.
61. Steiner, A.K.; Hunt, D.; Ho, S.-P.; Kirchengast, G.; Mannucci, A.J.; Scherllin-Pirscher-, B.; Gleisner, H.; von Engeln, A.; Schmidt, T.; Ao, C.; et al. Quantification of Structural Uncertainty in Climate Data Records from GPS Radio Occultation. *Atmos. Chem. Phys.* **2013**, *13*, 1469–1484. https://doi.org/10.5194/acp-13-1469-2013.
62. Khaykin, S.M.; Funatsu, B.M.; Hauchecorne, A.; Godin-Beekmann, S.; Claud, C.; Keckhut, P.; Pazmino, A.; Gleisner, H.; Nielsen, J.K.; Syndergaard, S. Postmillennium changes in stratospheric temperature consistently resolved by GPS radio occultation and AMSU observations. *Geophys. Res. Lett.* **2017**, *44*, 7510–7518. https://doi.org/10.1002/2017GL074353.
63. Leroy, S.S.; Ao, C.O.; Verkhoglyadova, O.P. Temperature trends and anomalies in modern satellite data: Infrared sounding and GPS radio occultation. *J. Geophys. Res. Atmos.* **2018**, *123*, 11431–11444. https://doi.org/10.1029/2018JD028990.
64. Steiner, A.K.; Ladstädter, F.; Randel, W.J.; Maycock, A.C.; Fu, Q.; Claud, C.; Gleisner, H.; Haimberger, L.; Ho, S.-P.; Keckhut, P.; et al. Observed Temperature Changes in the Troposphere and Stratosphere from 1979 to 2018. *J. Clim.* **2020**, *33*, 8165–8194. https://doi.org/10.1175/JCLI-D-19-0998.1.
65. Vergados, P.; Ao, C.O.; Mannucci, A.J.; Kursinski, E.R. Quantifying the Tropical Upper Tropospheric Warming Amplification Using Radio Occultation Measurements. *Earth Space Sci.* **2021**, *8*, e2020EA001597. https://doi.org/10.1029/2020EA001597.
66. Gleisner, H.; Lauritsen, K.B.; Nielsen, J.K.; Syndergaard, S. Evaluation of the 15-year ROM SAF monthly mean GPS radio occultation climate data record. *Atmos. Meas. Tech.* **2020**, *13*, 3081–3098. https://doi.org/10.5194/amt-13-3081-2020.
67. Gleisner, H.; Ringer, M.A.; Healy, S.B. Monitoring Global Climate Change Using GNSS Radio Occultation. *npj Clim. Atmos. Sci.* **2022**, *5*, 6. https://doi.org/10.1038/s41612-022-00229-7.
68. Ladstädter, F.; Steiner, A.K.; Gleisner, H. Resolving the 21st Century Temperature Trends of the Upper Troposphere-Lower Stratosphere with Satellite Observations. *Sci. Rep.* **2023**, *13*, 1306. https://doi.org/10.1038/s41598-023-28222-x.
69. Foelsche, U.; Syndergaard, S.; Fritzer, J.; Kirchengast, G. Errors in GNSS Radio Occultation Data: Relevance of the Measurement Geometry and Obliquity of Profiles. *Atmos. Meas. Tech.* **2011**, *4*, 189–199. https://doi.org/10.5194/amt-4-189-2011.

70. Shao, X.; Ho, S.-P.; Jing, X.; Zhou, X.; Chen, Y.; Liu, T.-C.; Zhang, B.; Dong, J. Characterizing the Tropospheric Water Vapor Spatial Variation and Trend Using 2007–2018 COSMIC Radio Occultation and ECMWF Reanalysis Data. *Atmos. Chem. Phys.* **2023**, *23*, 14187–14218. https://doi.org/10.5194/acp-23-14187-2023.
71. Rieckh, T.; Anthes, R.; Randel, W.; Ho, S.-P.; Foelsche, U. Evaluating Tropospheric Humidity from GPS Radio Occultation, Radiosonde, and AIRS from High-Resolution Time Series. *Atmos. Meas. Tech.* **2018**, *11*, 3091–3109. https://doi.org/10.5194/amt-11-3091-2018.
72. Zhang, H.; Kuo, Y.-H.; Sokolovskiy, S. Assimilation of Radio Occultation Data Using Measurement-Based Observation Error Specification: Preliminary Results. *Mon. Weather Rev.* **2023**, *151*, 589–601. https://doi.org/10.1175/MWR-D-22-0122.1.
73. Poli, P.; Healy, S.B.; Dee, D.P. Assimilation of Global Positioning System Radio Occultation Data in the ECMWF ERA–Interim Reanalysis. *Q. J. R. Meteorol. Soc.* **2010**, *136*, 1972–1990. https://doi.org/10.1002/qj.722.
74. Basha, G.; Kishore, P.; Ratnam, M.V.; Babu, S.R.; Velicogna, I.; Jiang, J.H.; Ao, C.O. Global Climatology of Planetary Boundary Layer Top Obtained from Multi-Satellite GPS RO Observations. *Clim. Dyn.* **2019**, *52*, 2385–2398. https://doi.org/10.1007/s00382-018-4269-1.
75. Kalmus, P.; Ao, C.O.; Wang, K.-N.; Manzi, M.P.; Teixeira, J. A high-resolution planetary boundary layer height seasonal climatology from GNSS radio occultations. *Remote Sens. Environ.* **2022**, *276*, 113037. https://doi.org/10.1016/j.rse.2022.113037.
76. Ho, S.-P.; Gu, G.; Zhou, X. The Planetary Boundary Layer Height Climatology over Oceans Using COSMIC-2 and Spire GNSS RO Bending Angles from 2019 to 2023: Comparisons to CALIOP, ERA-5, MERRA2, and CFS Reanalysis. *IEEE Trans. Geosci. Remote Sens.* **2024**, *62*, 5803314. https://doi.org/10.1109/TGRS.2024.3503418.
77. Ho, S.-P.; Peng, L.; Anthes, R.A.; Kuo, Y.-H.; Lin, H.-C. Marine Boundary Layer Heights and Their Longitudinal, Diurnal, and Interseasonal Variability in the Southeastern Pacific Using COSMIC, CALIOP, and Radiosonde Data. *J. Clim.* **2015**, *28*, 2856–2872. https://doi.org/10.1175/JCLI-D-14-00238.1.
78. Ao, C.O.; Waliser, D.E.; Chan, S.K.; Li, J.-L.; Tian, B.; Xie, F.; Mannucci, A.J. Planetary boundary layer heights from GPS radio occultation refractivity and humidity profiles. *J. Geophys. Res.* **2012**, *117*, D16117. https://doi.org/10.1029/2012JD017598.
79. Xie, F.; Wu, D.L.; Ao, C.O.; Mannucci, A.J.; Kursinski, E.R. Advances and limitations of atmospheric boundary layer observations with GPS occultation over southeast Pacific Ocean. *Atmos. Chem. Phys.* **2012**, *12*, 903–918. https://doi.org/10.5194/acp-12-903-2012.
80. Chan, K.M.; Wood, R. The Seasonal Cycle of Planetary Boundary Layer Depth Determined Using COSMIC Radio Occultation Data. *J. Geophys. Res. Atmos.* **2013**, *118*, 12422–12434. https://doi.org/10.1002/2013JD020147.
81. Gorbunov, M.E.; Lauritsen, K.B. Analysis of Wave Fields by Fourier Integral Operators and Their Application for Radio Occultations. *Radio Sci.* **2004**, *39*, RS4010. https://doi.org/10.1029/2003RS002971.
82. Gorbunov, M.E.; Lauritsen, K.B.; Rhodin, A.; Tomassini, M.; Kornblueh, L. Radio Holographic Filtering, Error Estimation, and Quality Control of Radio Occultation Data. *J. Geophys. Res. Atmos.* **2006**, *111*, D10105. https://doi.org/10.1029/2005JD006427.
83. Sokolovskiy, S.; Rocken, C.; Schreiner, W.; Hunt, D. On the uncertainty of radio occultation inversions in the lower troposphere. *J. Geophys. Res.* **2010**, *115*, D22111. https://doi.org/10.1029/2010JD014058.
84. Paolella, S.; von Engeln, A.; Padovan, S.; Notarpietro, R.; Marquardt, C.; Sancho, F.; Rivas Boscan, V.; Morew, N.; Martin Alemany, F. Assessment of Operational Non-Time-Critical Sentinel-6A Michael Freilich Radio Occultation Data: Insights into Tropospheric GNSS Signal Cut-Off Strategies and Processor Improvements. *Atmos. Meas. Tech.* **2025**, *18*, 2825–2846. https://doi.org/10.5194/amt-18-2825-2025.
85. Vannah, S.; Leroy, S.S.; Ao, C.O.; Kursinski, E.R.; Nelson, K.J.; Wang, K.-N.; Xie, F. The Impact of Differences in Retrieval Algorithms between Processing Centers on GNSS Radio Occultation Refractivity Retrievals in the Planetary Boundary Layer. *Atmos. Meas. Tech.* **2025**, *18*, 4293–4310. https://doi.org/10.5194/amt-18-4293-2025.
86. Sokolovskiy, S. Effect of superrefraction on inversions of radio occultation signals in the lower troposphere. *Radio Sci.* **2003**, *38*, 1058. https://doi.org/10.1029/2002RS002728.
87. Xie, F.; Wu, D.L.; Ao, C.O.; Kursinski, E.R.; Mannucci, A.J.; Syndergaard, S. Super-refraction effects on GPS radio occultation refractivity in marine boundary layers. *Geophys. Res. Lett.* **2010**, *37*, L11805. https://doi.org/10.1029/2010GL043299.
88. Feng, X.; Xie, F.; Ao, C.O.; Anthes, R.A. Ducting and biases of GPS radio occultation bending angle and refractivity in the moist lower troposphere. *J. Atmos. Ocean. Technol.* **2020**, *37*, 1013–1025. https://doi.org/10.1175/JTECH-D-19-0206.1.
89. Sokolovskiy, S.; Zeng, Z.; Hunt, D.C.; Weiss, J.-P.; Braun, J.J.; Schreiner, W.S.; Anthes, R.A.; Kuo, Y.-H.; Zhang, H.; Lenschow, D.H.; et al. Detection of Superrefraction at the Top of the Atmospheric Boundary Layer from COSMIC-2 Radio Occultations. *J. Atmos. Ocean. Technol.* **2024**, *41*, 65–78. https://doi.org/10.1175/JTECH-D-22-0100.1.

90. Wang, K.-N.; de la Torre Juárez, M.; Ao, C.O.; Xie, F. Correcting Negatively Biased Refractivity below Ducts in GNSS Radio Occultation: An Optimal Estimation Approach towards Improving Planetary Boundary Layer (PBL) Characterization. *Atmos. Meas. Tech.* **2017**, *10*, 4761–4776. https://doi.org/10.5194/amt-10-4761-2017.
91. Wang, K.-N.; Ao, C.O.; de la Torre Juárez, M. GNSS-RO refractivity bias correction under ducting layer using surface-reflection signal. *Remote Sens.* **2020**, *12*, 359. https://doi.org/10.3390/rs12030359.
92. Parde, A.N.; Oikonomou, C.; Haralambous, H. Enhancing GNSS Water Vapour Retrieval via Synergistic Microwave Radiometry: Thermodynamic Error Diagnosis and Bias Correction. *Atmos. Meas. Tech.* **2026**, *19*, 4517–4537. https://doi.org/10.5194/amt-19-4517-2026.
93. Xie, F.; Syndergaard, S.; Kursinski, E.R.; Herman, B.M. An approach for retrieving marine boundary layer refractivity from GPS occultation data in the presence of super-refraction. *J. Atmos. Ocean. Technol.* **2006**, *23*, 1629–1644. https://doi.org/10.1175/JTECH1996.1.
94. Maier, M.W.; Gallagher, F.W.I.I.I.; St Germain, K.; Anthes, R.; Zuffada, C.; Menzies, R.; Piepmeier, J.; Di Pietro, D.; Coakley, M.M.; Adams, E. Architecting the future of weather satellites. *Bull. Am. Meteorol. Soc.* **2021**, *102*, E589–E610. https://doi.org/10.1175/BAMS-D-19-0258.1.

Disclaimer/Publisher's Note: The statements, opinions and data contained in all publications are solely those of the individual author(s) and contributor(s) and not of MDPI and/or the editor(s). MDPI and/or the editor(s) disclaim responsibility for any injury to people or property resulting from any ideas, methods, instructions or products referred to in the content.